学位論文（要約）

First-Principles Simulation of the Ionic Conduction in Mixed Anion Compounds

（複合アニオン化合物における
イオン伝導の第一原理シミュレーション）

平成 28 年 12 月博士（理学）申請

東京大学大学院理学系研究科

化学専攻

岡　真悠子

First-Principles Simulation of the Ionic Conduction in Mixed Anion Compounds

by

Mayuko Oka

Department of Chemistry
Graduate School of Science
The University of Tokyo

December 2016

Abstract

Solid-state ionic conductors are widely used as ionic sensors or electrolytes for fuel cells and secondary batteries. As the performance of such devices heavily relies on the ionic conductivity of these materials, and to expand the application fields of the devices, investigation of new ionic conductive materials is one of the most important issues in the chemical industry. Fluorite with composition of MX_2 is a typical mother structure of ionic conductors. However, there are many kinds of polymorphs of which phase stability depends on the ratio of ionic radii (r_{cation}/r_{anion}), and/or ordering of ions. Doping of aliovalent ions generates compensating cation/anion vacancies, which also affects the crystal structure of compounds. In this thesis, I focused on two materials having fluorite structure, ZrO_2 and LaOF. From the first-principles simulation, I discussed the mechanism of ionic conduction and explored the keys to control their properties.

In preceding literatures, several factors were proposed to enhance the ionic conductivity besides the concentration of conducting carrier: mixed bonding character (such as ionicity/covalency) and properties of the mobile and immobile ions (charge, size, polarizability, etc). Recently, epitaxial strain at the interface of multilayer thin film has been intensively studied because of their potential for higher ionic conductivity. In particular, $(ZrO_2)_{0.92}(Y_2O_3)_{0.08}$ (8YSZ)/$SrTiO_3$ heteroepitaxial structure has attracted much attention for its anomalously high oxide ion conductivity, although the reproducibility of the phenomenon is still under debate.

In this thesis, I first investigated the mechanism of the ionic conduction in ZrO_2 systems under tensile epitaxial strain. I conducted density functional perturbation theory (DFPT)-based phonon calculations to determine the dynamically stable structure. The cell was expanded along the *a*- and *b*-axes to match the lattice constant for $SrTiO_3$ with a 45° rotation (about 7% tensile strain), and thus to reproduce the epitaxial strain in the YSZ/$SrTiO_3$ multilayer. By tensile epitaxial strain, the oxygen sublattice of pure ZrO_2 was dramatically changed into the zigzag structure, as suggested in the preceding studies. This structure has the space group of *Pbcn*, which was precisely determined by phonon calculation in this study. *Ab initio* MD simulations were performed initiating from the dynamically stable structure. The following models were constructed; (1) 1 oxygen vacancy (V_O) ($Zr_{72}O_{143}\square$, where $\square$ denotes V_O); (2) $6V_O$ and no Y^{3+} dopant ($Zr_{72}O_{138}\square_6$); (3) $6V_O$ and compensating Y^{3+} ions ($Zr_{60}Y_{12}O_{138}\square_6$, represents YSZ). No significant increase in the MSD was observed in $1V_O$ system when starting from the dynamically stable structure. The ionic conductivity was remarkably increased when the tensile strain and several oxygen vacancies were introduced simultaneously (model (2) or (3)). The conductivity was almost dominated by the number of oxygen vacancies. These oxygen vacancies seemingly deformed the spatial oxygen ordering state, which led to the enhancement of the oxide ion conductivity. The present results indicate that the oxide ion conductivity in ZrO_2 is largely influenced by the oxygen ordering pattern, which sensitively changes with the lattice strain and the number of oxygen vacancies.

In this context, anion doping into anion sublattice of ZrO_2 could also affect the oxide ion conductivity since these dopants will be directly incorporated into the mobile sublattice rather than the cation counterpart. Next, I discussed the effect of N/F-doping into tensile-strained ZrO_2, particularly focusing on the structural change of oxygen sublattice. The effect of N/F-doping was further analyzed referring to the strengths of Zr–O bonds using Crystal Orbital Hamilton Population (COHP) analysis. Several models with different concentrations of oxygen vacancies were compared; (4) $1V_O$ and 3 N/F-doping ($Zr_{72}O_{140}N_3\square$ and $Zr_{72}O_{140}F_3\square$); (5) $3V_O$ and 3 N/F-doping ($Zr_{72}O_{138}N_3\square_3$ and $Zr_{72}O_{138}F_3\square_3$); (6) $6V_O$ and 3 N/F-doping ($Zr_{72}O_{135}N_3\square_6$ and

$Zr_{72}O_{135}F_3\square_6$). The zigzag structure was perturbed by the flipping motion of the lattice at low concentration of dopants or vacancies, and, with increasing the concentration, it was broken into a fluid-like state. Besides, chemical bonding analysis of Zr−O showed that the bonds near the vacancies was weakened by F- or V_O-doping and strengthened by N-doping. Despite the opposite effects on the nearby Zr−O bonds, all doping commonly enhanced the ionic conduction; the doped F^- or V_O directly weakened the Zr–O bonds in its vicinity, whereas the N^{3-} strengthened the Zr–O bonds in its vicinity but weakened other Zr–O bonds and thus promoted the ionic conduction. Additionally, I observed a peculiar migration mechanism, which is similar to the vacancy mechanism but is mediated by the interstitial position. This migration mechanism *via* interstitial site might be easier to occur in the in-plane direction than in the out-of-plane, since the interstitial site is opened along the in-plane direction by the tensile strain. This novel conduction mechanism involving interstitial sites, which were induced by tensile strain, supposedly contributed to the enhanced ionic conductivity in ZrO_2 systems.

Finally, I explored the ionic conduction mechanism on a mixed anion compounds LaOF, which shows fluoride ion conduction with high selectivity. The anions of LaOF show different ordered structures, a rhombohedral (*R-3m*, [111] ordering) or tetragonal structure (*P4/nmm*, [001] ordering) depending on its non-stoichiometry, where the latter structure is usually obtained in fluorine-excess condition ($LaO_{1-x}F_{1+2x}$, $x > 0$). In general, ionic conduction mechanism can be classified into interstitial, interstitialcy, or vacancy mechanism. Experimental studies suggested that interstitial fluoride ion is the main carrier species in LaOF. However, precise discussion on the selectivity and mechanism of fluoride ion conduction has not been made so far. In this study, I investigated the diffusion mechanism of fluoride ion in LaOF from theoretical perspectives. The formation of F Frenkel pair was more energetically favored than O

Frenkel pair by more than 1.7 eV, which suggests that the F Frenkel pair contributes to the fluoride ion conduction. *Ab initio* MD simulations revealed that the fluoride ion conduction was mainly mediated by the interstitialcy mechanism. Interestingly, such interstitialcy mechanism of interstitial fluoride ion occurred along (001) plane only when its nearest anion sites on the (001) plane are occupied by fluoride ions. The present finding, i.e., dominance of the interstitialcy mechanism under a restricted condition, suggests that the ionic conductivity of mixed anion compounds can be enhanced by controlling the anion ordering.

Acknowledgement

In the first place, I would like to express my sincere appreciation and gratitude to my supervisor Prof. Tetsuya Hasegawa. His advice always led me to improve and deepen the research. I want to express my great gratitude to Prof. Tomoteru Fukumura, who always gave me important advice and scientific interest with a bit of humor, even after he moved to Tohoku University. I gratefully thank Dr. Hideyuki Kamisaka for essential theoretical guidance and technical advice. When I changed my theme and started the theoretical study in my master course, I have known little about calculation. He gave me a lot of advices about theoretical background and computational procedure. I also gratefully thank to Prof. Yasushi Hirose for great scientific advice. He helped me a lot especially when I engaged in my research at KAST in my bachelor course. I gratefully thank to Dr. Akira Chikamatsu for encouraging me to improve the motivation for my study.

In my doctor course, I have many opportunities to discuss with other researchers at conferences, workshops, JST-CREST meetings, and so on. I have received much advice, which helped me a lot for improving my study. I gratefully thank Prof. T. Fujiwara, Prof. T. Hoshi, Dr. M. Ikeda, and Dr. S. Nishino for their helpful discussions. I also gratefully thank Prof. K. Tamao, the adviser of JST-CREST project, for encouraging the scientific interest. I also appreciate the computational support by the Research Center for Computational Science, Okazaki, Japan.

I thank present and past members of calculation group for gave me important advice about this study: Mr. Y. Kurauchi, Mr. N. Hashimoto, Mr. Koki Kawahara, Mr. T. Koizumi, Mr. S. Mo, and Mr. T. Wakasugi. I am also thankful to present and past member of Hasegawa laboratory: Mr. S. Nakao, Dr. S.Okazaki, Dr. C.Yang, Dr. Y. Park, Dr. D. Ogawa, Dr. A. Watanabe, Dr. J. Wei, Dr. D. Oka, Dr. K. Shigematsu, Mr.

T. Kawashima, Dr. T. Katayama, Dr. T. S. Krasienapibal, Dr. J. Il, Dr. A. Suzuki, Dr. S. Kojima, Mr. K. Aizawa, Dr. K. Shimamoto, Ms. M. Otaki, Ms. X. Shen, Mr. S. Inoue, Mr. R. Sei, Ms. K. Kurita, Mr. R. Takagi, Mr. T. Onozuka, Mr. M. Sano, Mr. K. Kaminaga, Mr. J. Takahashi, Mr. K. Yamatake, Mr. V. Motaneeyachart, Mr. D. Kutsuzawa, Mr. Keissuke Kawahara, Mr. F.S. Kahn, Mr. Y. Uchida, Mr. T. Yamazaki, Mr. R. Kantake, Mr. T. Takeda, Mr. Y. Suzuki, Mr. S. Shibata, Mr. N. Kashiwa, Mr. Keisuke Yamada, Mr. K. Maruyama, Mr. S. Fujiwara, Mr. T. Fukumoto, Mr. T. Shiina, Ms. Y. Zhu, Mr. S. Tanaka, Mr. K. Hayahara, and Mr. Kuni Yamada. I also thank present and past secretaries of Hasegawa group: Ms. M. Umino, Ms. M. Komazawa, Ms. A. Imoji, and Ms. M. Kikuchi.

I am deeply grateful to all of the professors in the chemistry department. They taught me what chemistry is from the very fundamental point. I also thank my classmates in chemistry department for studying together and continuous encouraging each other.

Finally, I have to express my deepest gratitude to my family for their warm encouragements and continuous supports.

Contents

Chapter 1

General introduction 1

1.1 Solid state ionic conductors 1

1.2 Kinds of ionic conducting compounds 9

1.3 Social demands for ionic conductors 13

1.4 How to measure the ionic conductivity 18

1.5 Advantages of theoretical calculation 22

1.6 Purpose of this study 23

Chapter 2

Calculation method 24

2.1 Concept of theoretical calculation 24

2.2 Density functional theory (DFT) 24

2.3 Density functional perturbation theory (DFPT) 27

2.4 Formation energy of Frenkel pair 28

2.5 Molecular Dynamics (MD) simulation 29

2.6 Evaluation of the ionic conductivity 31

2.7 Evaluation of the bonding character 32

2.8 Evaluation of the migration barrier 34

Chapter 3

Phonon calculation and *ab initio* MD simulation of ZrO_2 systems under epitaxial strain 36

3.1 Introduction 36

3.2 Calculation method 39

3.3 Results and discussion 41

3.4 Summary of this chapter 51

Chapter 4

Ab initio MD simulation of N/F-doped ZrO_2 under epitaxial strain........................... 53
4.1 Introduction 53
4.2 Calculation method 54
4.3 Results and discussion 55
4.4 General discussion about ZrO_2 systems 67
4.5 Summary of this chapter 71

Chapter 5

DFT-based first-principles simulations of LaOF 73
5.1 Introduction 73
5.2 Calculation method 75
5.3 Results and discussion 77
5.4 Summary of this chapter 90

Chapter 6

General conclusion 92
Bibliography 95

Chapter 1 General introduction

1.1 Solid state ionic conductors

Solid-state ionic conductors are widely used as ionic sensors or electrolytes for fuel cells and secondary batteries. From the view point of solid state chemistry, such ionic conductors are quite interesting because they have much room for designing their properties, such as selection of mother compound, doping elements, both anions and cations, and ordering of ions. Lattice strain is also an important parameter affecting the ionic conduction behavior. By controlling these parameters, it is possible to design the conducting path and conducting ionic species. Certainly, the primary goal for investigating the ionic conducting materials is to improve the ionic conductivity. As is generally assessed, the ionic conductor has ionic conductivity more than 10^{-2}–10^{-3} $\mathrm{Scm^{-1}}$. This ionic conducting state is also called as "superionic" state, where the ions can transfer extensively as liquid state does even below the melting temperature.

1.1.1 Fundamental properties of ionic conductors

Until now, many ionic compounds have been reported as either cation or anion conductors. As a general tendency, ionic conduction is higher when the ions have a smaller radius or a smaller charge. In reality, however, there are many examples that do not follow the above-mentioned simple tendency. This motivates us to design new ionic conducting materials.

In this section, I will briefly describe the fundamental understanding of ionic conducting materials by referring to α-AgI and β-PbF_2 as typical examples [1]. These two materials exhibit opposite behaviors in fundamental properties, as follows.

(1) Cation / anion conductors

First, conducting species are different; cation diffuses in α-AgI, while anion does in β-PbF_2. In α-AgI, smaller ion Ag^+ (r = 1.14 Å in coordination number (CN) of 4, Shannon's crystal radius was adopted for all the data in the text hereafter [2]) would migrate easier than larger ion I^- (r = 2.06 Å [2]), as expected from the general tendency. The actual mechanism for its high ionic conductivity is more complicated.

In α-AgI, I^- ions form a body-centered cubic (bcc) sublattice, where Ag^+ ions occupy either two of six octahedral, twelve tetrahedral or twenty-four trigonal interstitials in the unit cell. These sites are illustrated in Fig. 1-1.

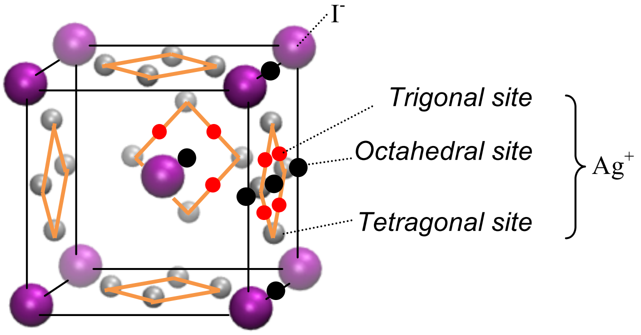

Fig. 1-1 Crystal structure and its anion sites of α-AgI. Only tetragonal sites are illustrated in the structure, where octahedral sites and trigonal sites are added as black and red circles. The front surface is omitted for clear appearance.

Because of the presence of many unoccupied sites, α-AgI shows a good ionic conductivity. This structure of α-AgI is expressed as liquid-like structure [1]. In addition, the bonding character of α-AgI fluctuates in time between covalent bond and ionic bond depending on the Ag^+ site [3].

The structure shown in Fig. 1-1, and all the structures hereafter, including trajectories of the ionic motions (in Chapter 3, 4 and 5), were reproduced by VMD software; W. Humpjrey, A. Dalke and K. Schulten, J. Mol. Graphics **14**, 33 (1996). http://www.ks.uiuc.edu/Research/vmd/.

This mixed bonding character is suggested to be characteristic of good ionic conductors.

The situation is totally different in β-PbF_2, which shows anion conductivity. The ionic radius (r_{Pb2+} = 1.43 Å (CN = 8) > r_{F-} = 1.17 Å (CN = 4) [2]) and the charge of respective ions (Pb^{2+} and F^-) suggest the fluoride ion conduction in this compound. Indeed, fluoride ion conduction was confirmed by comparing the defect formation energy; cation defect formation energy is relatively high in this compound [1]. The defect formation energy is an important parameter for the ionic conductivity because the ionic conductors need some ‘carriers’ such as excess interstitial ion or vacancy, as will be explained in Section 1.1.2. In case of β-PbF_2, Frenkel pair is the most dominant carrier for fluoride ion conduction, which is described as $F_F^{\times} \rightarrow V_F^{\bullet} + F_i^{\prime}$ in Kröger-Vink notation. Fig. 1-2 illustrates the structure of β-PbF_2, which forms the cubic fluorite structure. When focusing on the anion framework, one can see that the cations occupy every other site of octahedron as depicted in Fig. 1-2(b). Consequently, there exist empty interstitial sites in the structure.

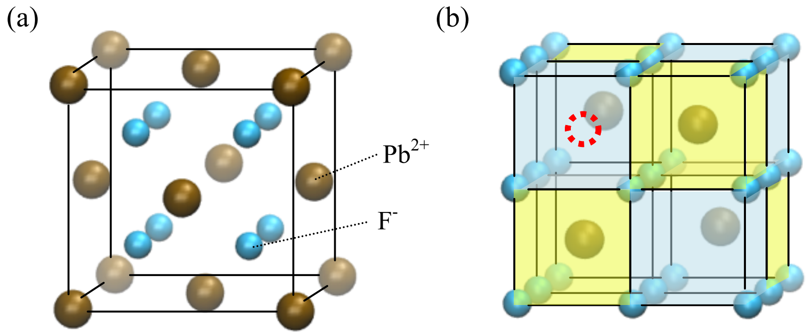

Fig. 1-2 (a) Fluorite structure. (b) Anion framework of the same structure. The small octahedra with different colors show Pb^{2+} (yellow) or empty (blue) site. Red dashed circle shows the interstitial position of F^- in cube center (position F4 in the main text).

In preceding studies, the position of interstitial sites was discussed [1]. There are mainly four possible positions for interstitial anions in β-PbF_2. Position F4 locates the cube center (red circle in Fig. 1-2(b)), and F1, F2, F3 locates the intermediate positions of F4 in [110] (F1 at 1/2) or [111] (F2 at 1/2, F3 at 1/4) direction. At low temperature, interstitial anion occupies F4 position. On the other hand, at high temperature, F1 and F2 sites are filled rather than F4 position. These interstitial fluoride ions contribute to the ionic conduction of this compound. The conduction mechanisms of other fluorite compounds, such as CaF_2, are similar to β-PbF_2.

(2) Type-I and type-II transitions

Similar to superconducting materials, phase transition into superionic materials can be classified into type-I (abrupt) or type-II (continuous) transitions. Ionic conductivity is often described as a function of inverse temperature, which is referred to as Arrhenius plot (log σ versus $1/T$). α-AgI is classified as type-I, where the structure drastically changes into super ionic phase. Thus, the Arrhenius plot has discontinuity or abrupt drop/increase at transition temperature T_c. On the other hand, β-PbF_2 is classified as type-II, where the ionic conductivity gradually increases without definite transition point. Since the transition is accompanied with λ-peak in specific heat C_p, the maximum of C_p is defined as T_c conveniently [1]. The T_c of β-PbF_2 is estimated at 711 K [4]. It is interesting to note that the T_c of β-PbF_2 is significantly lower than those of other fluorite compounds (1430 K for CaF_2 [1]). This may be due to high polarizability of Pb^{2+} arising from $6s^2$ lone-pair electrons [1]. Another example of lone-pair electrons is Bi^{3+} [5]. Many studies have been made on the Bi^{3+}-based materials, such as $BiMeVO_x$ (Me = metal cations) families [6] and $K_{1-x}Bi_xF_{1+2x}$ [7].

Consequently, the possible factors affecting the ionic conductivity can be summarized, as follows [1]:

- smaller radius and smaller charge (general tendency)
- many unoccupied (interstitial) sites
- lower defect formation energy

- mixed bonding character (such as ionic-covalent)
- high polarizability

By controlling these factors or even finding a new factor, it will be possible to increase the ionic conductivity of the material.

1.1.2 Carrier of ionic conductors

As mentioned in the previous section, there must be some carriers that mediate the ionic diffusion in ionic conductors. The carrier is either interstitial ion or vacancy. In actual ionic conductors, such carriers move according to the concentration gradient of ion or the external electric field. The next concern is how to generate such carries. In general, ionic conductors can be classified into two types in terms of the carrier generation mechanism.

(1) Intrinsic ionic conductors

In intrinsic ionic conductors, their chemical compositions are generally stoichiometric. In this case, Frenkel pairs (as in the case of β-PbF_2 in Section 1.1.1) generated by thermal excitation carry charges. The Frenkel pair consists of the interstitial ion and vacancy, as illustrated in Fig. 1-3.

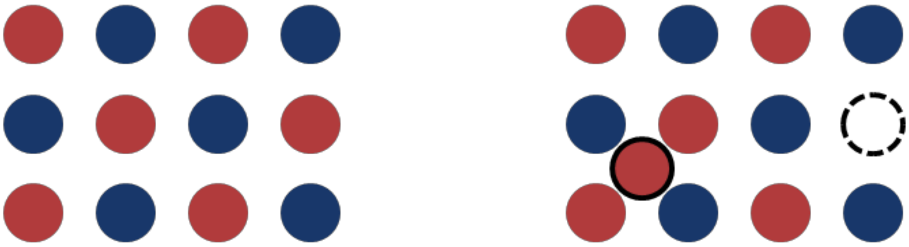

Fig. 1-3 Schematic of Frenkel pair; (a) Perfect crystal (b) Crystal with one Frenkel pair.

The concentration of Frenkel pair C_s is estimated by the following equation [8]:

$$C_s = \sqrt{(NN')} \exp(-W_F/2k_BT) / N_A, \tag{1-1}$$

where N and N' is the concentrations of lattice and interstitial sites, respectively, N_A is

Avogadro's number, and W_F is the Frenkel pair formation energy.

(2) Extrinsic ionic conductors

In this type of ionic conductors, the conducting carriers are generated by extrinsic causes, such as doping of aliovalent cations or anions, as schematically illustrated in Fig. 1-4.

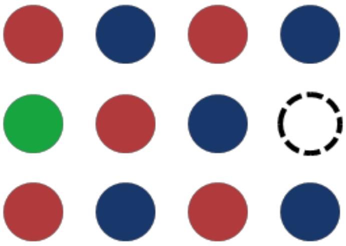

Fig. 1-4 Schematic of cation or anion doping. Vacant counterparts are generated, at the same time, due to the charge neutrality.

When aliovalent cations or anion were doped into the system, vacant counterpart will be generated due to the charge neutrality. A typical example is doped ZrO_2, where lower valent cations, such as Y^{3+}, Sc^{3+} and Ca^{2+}, are substituted for Zr^{4+} [9][10]. Oxygen vacancy is generated to compensate the doped cation, as expressed by the Kröger-Vink notation as follows:

$$Y_2O_3 \xrightarrow{ZrO_2} 2Y_{Zr}' + V_O^{\cdot\cdot} + 3O_O^{\times} \qquad (1\text{-}2)$$

$$CaO \xrightarrow{ZrO_2} Ca_{Zr}'' + V_O^{\cdot\cdot} + O_O^{\times}. \qquad (1\text{-}3)$$

The ionic conducting properties are significantly different from a dopant to another even when the dopants have the same valence, and thus the choice of dopant is an interesting issue to be investigated [9].

1.1.3 Diffusion mechanism

In general, there are mainly three kinds of ionic conduction mechanisms: interstitial, interstitialcy, and vacancy mediated conduction. These mechanisms are schematically shown in Fig. 1-5.

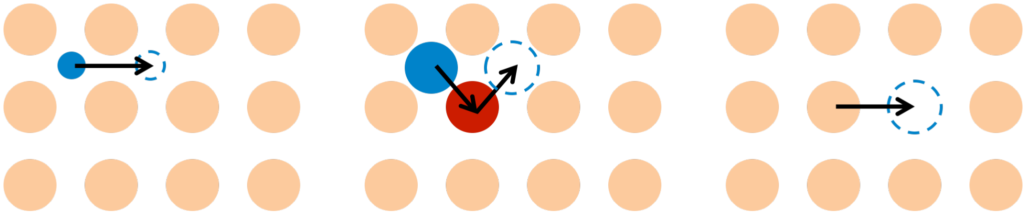

Fig. 1-5 Three kinds of ionic conduction mechanisms: (from the left) interstitial, interstitialcy, and vacancy mechanisms.

These mechanisms are briefly explained as follows [11].

(1) Interstitial mechanism (direct interstitial mechanism)

In this type of diffusion mechanism, the interstitial ion simply hops between the sites. Since this mechanism does not involve any other ions or vacancies, the diffusion coefficient is generally high if the interstitial ions are small enough to pass through.

(2) Interstitialcy mechanism (indirect interstitial mechanism)

In this mechanism, the carrier is also the interstitial ion (Fig. 1-5, blue ion) but the interstitial ion 'kicks out' the site ion (Fig. 1-5, red ion) and the kicked-out ion goes into the interstitial site, instead. This mechanism is advantageous for relatively large ions, because the lattice distortion by the interstitial ion would be less significant compared to interstitial mechanism.

(3) Vacancy mechanism

In this mechanism, the site ion diffuses *via* the vacancy. In the actual system with higher concentration of vacancies, clustering or ordering of these vacancies frequently takes place [12], which is an important factor when discussing the ionic conductivity of the materials.

1.1.4 Random walk theory

In any diffusion mechanisms in Section 1.1.3, the diffusion of individual ions can be simply described by either going forth or going back. This situation is treated in random walk theory as follows [11].

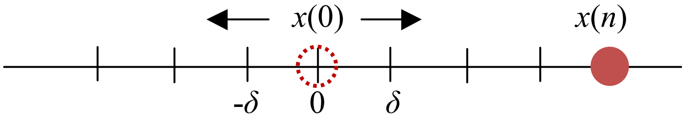

Fig. 1-6 Schematic of random walk theory in 1D.

The position of ion after n-th jump will be $x(n) = x(n\text{-}1) \pm \delta$ (δ: distance for single jump), and its mean square displacement (MSD) will be

$$< x^2(n) > = < x^2(n\text{-}1) \ \pm 2\, x(n\text{-}1)\, \delta + \delta^2 > = < x^2(n\text{-}1) > + \, \delta^2. \qquad (1\text{-}4)$$

From the initial condition of $x(0) = 0$, one can obtain

$$< x^2(1) > = \delta^2, < x^2(2) > = \delta^2 + \delta^2 = 2\delta^2 \text{ , … } < x^2(n) > = n\, \delta^2 = (\delta^2/\tau)\, t, \qquad (1\text{-}5)$$

where $n = 1/\tau$ is the jump frequency. Since δ and τ are constant values, the MSD is proportional to time, where its slope represents the magnitude of diffusion.

It is not difficult to expand this treatment from 1D to 3D system, and, finally, the MSD can be described as MSD = $6Dt$ + const., where D is the diffusion coefficient, being a measure for ionic conductivity. The above treatment will be used in Chapter 3, 4, and 5.

1.1.5 Correlation factor

As seen in Section 1.1.3, some diffusion mechanisms involve other ions. In such cases, the diffusion coefficient depends on the concentration of carriers. That is, at a higher carrier concentration, the carriers are no longer independent and feel correlation. Thus, the diffusion coefficient at higher carrier concentration differs from the simple summation of individual diffusion derived from the random walk theory. This difference is quantified by the correlation factor f, which related the observed diffusion coefficient D and self-diffusion coefficient D_s as $D = f D_s$.

In the case of interstitial mechanism, $f = 1$ since the diffusion of interstitial ion does not involve other ions [11].

In the case of interstitialcy or vacancy mechanism, f is smaller than 1, since these mechanisms involve other ions. Furthermore, the value of f can be estimated from the crystal structure if diffusion mechanism is specified [11][13][14]. It is possible to determine the diffusion mechanism from the correlation factor evaluated by combining experimental data (will be described in Section 1.4).

1.2 Kinds of ionic conducting compounds

To date, many compounds are known to exhibit ionic conductivity. These include doped CeO_2, Y_2O_3-stabilized ZrO_2 (YSZ), and doped $LaGaO_3$ for O^{2-}; LaF_3, β-PbF_2, CaF_2 for F^- ; doped-$SrCeO_3$ for H^+ ; LISICON or NASICON for Li^+ or Na^+ [15]. Recent extensive studies led to the discovery of novel ionic conducting materials [16][17]. In this section, the ionic conducting compounds are classified by their structures or conducting paths.

1.2.1 Fluorite structure

As explained in Section 1.1.1 about β-PbF_2, fluorite structure is one of the most typical mother structures for ionic conductors. Representative materials are PbF_2, CaF_2, BaF_2, CeO_2, yttria stabilized ZrO_2 (YSZ), and so on.

Fluorite compounds have the same composition of MX_2, however, other polymorphs could be stabilized depending on the ratio of ionic radii (r_{cation}/r_{anion}) and/or ordering of ions. For example, ZrO_2 has three polymorphs aside from fluorite structure: monoclinic ($P2_1/c$, < 1400 K), tetragonal ($P4_2/nmc$, 1400–2600 K). Fluorite structure (*Fm-3m*) appears only at high temperature (> 2600 K) [18]. Doping aliovalent cations into ZrO_2 not only introduces oxygen vacancies, but also stabilizes the fluorite structure at lower temperature. On the other hand, doping aliovalent cations into CeO_2 only plays a role in introducing oxygen vacancies since pristine CeO_2 takes the fluorite structure in the entire temperature region [19]. Interestingly, how the charge of aliovalent cation dopant is compensated depends on the cation radius. Doping of relatively small Al^{3+}, Sc^{3+} or In^{3+} into CeO_2 produces oxygen vacancies to compensate the charge of dopant. In contrast, doping large cations, such as Y^{3+} or La^{3+} causes the reduction of Ce valence from 4+ to 3+ [20].

Mixed anion fluorite compounds, rare-earth oxyfluorides LnOF (Ln = lanthanides), have also been reported as ionic conductors. In LnOF, the cations form the cubic fluorite sublattice. The anions, fluoride and oxide ions, take a different crystal structure depending on its non-stoichiometry. If the oxide and fluoride ions order along the [111] direction of the cation sublattice, a rhombohedral structure (*R-3m*) is observed [21][22]. When the ordering changes to [001] direction of the cation sublattice, a tetragonal structure (*P4/nmm*) is obtained [23][24]. The latter structure tends to be obtained in fluorine-excess condition ($LnO_{1-x}F_{1+2x}$, $x > 0$). At high temperature, both structures undergo order-disorder transformation into F/O-disordered cubic structure (*Fm-3m*) [23][24].

As for the ionic conducing carriers, both interstitial ion and vacancy have been reported in fluorite structure. For example, the ionic conduction in ZrO_2 or CeO_2 is mediated by the vacancy mechanism. Recent theoretical simulations confirmed the diffusion mechanism in ZrO_2 and CeO_2 to be vacancy-type by comparing different diffusion mechanisms [25][26]. In case of a fluoride ion conductor CaF_2, several experimental studies have shown that both vacancy and interstitial fluoride ion contribute to the ionic conduction, and concluded that the interstitial one is crucial for the ionic conduction [27]. It is also reported that the interstitial F rapidly exchanges with lattice F, supporting the interstitialcy diffusion mechanism [28].

Thus, fluorite compounds have several possible polymorphs and their ionic conduction mechanisms depend on the ionic radius or species. The fluorite structure is worth investigating from the viewpoint of fundamental diffusion mechanisms as well as cation/anion framework for high ionic conductivity.

1.2.2 Perovskite structures

Perovskite structure consists of anion octahedra surrounding central cation *B* and larger cation *A* sustaining the framework. The composition can be formulated as ABX_3 (A = large cation, B = small cation, X = anion).

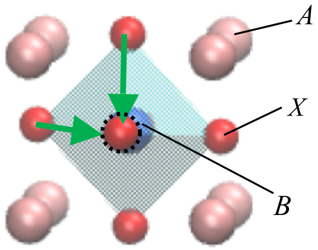

Fig. 1-7 Perovskite structure and vacancy mechanism (green arrows).

A representative ionic conductor with this structure is doped-$LaGaO_3$ (e.g. $La_{0.9}Sr_{0.1}Ga_{0.8}Mg_{0.2}O_{3-\delta}$ [29]). Vacancy mechanism is suggested in this perovskite compound, as shown in Fig. 1-7 [30].

1.2.3 Ruddlesden–Popper structures

The Ruddlesden–Popper structure is described as the chemical formula of A_2BX_4. This structure can be regarded as stacking of perovskite (ABX_3) and rock-salt (AX) blocks along the *c*-axis (Fig. 1-8).

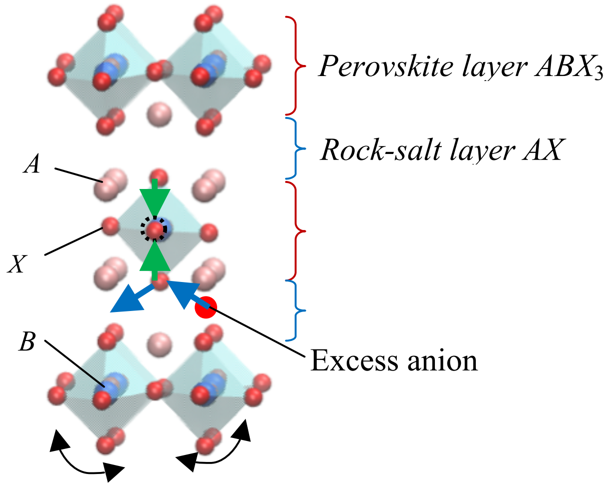

Fig. 1-8 Ruddlesden–Popper structures. Green arrows: vacancy mechanism, blue arrows: interstitialcy mechanism, black arrows: octahedral rotation.

There are two proposed mechanisms in this structure; one is vacancy mechanism in perovskite layer (greens arrow in Fig. 1-8), the other is interstitialcy mechanism between excess anion in rock-salt layer and apical anion in perovskite layer (blue arrows) [31]. The former mechanism is observed in anion-deficient $ABX_{4-\delta}$, while the latter is seen in anion-excess $ABX_{4+\delta}$, The anion-deficient or excess state can be achieved by doping an aliovalent cation into *A* or *B* site, as seen in oxygen-deficient $Sr_2(Ti, Co)O_{4-\delta}$ and oxygen-excess $Pr_2(Ni, Cu)O_{4+\delta}$ and $(La,Sr)_2CoO_{4+\delta}$ and so on [32][33].

In this type of compounds, the ionic conductivity of interstitial anion through interstitialcy mechanism is generally higher than vacancy-mediated diffusion [32]. It is interesting to note that the interstitialcy diffusion is accompanied with octahedral rotation of the perovskite layer (black arrows in Fig. 1-8) [34]. It is reported that the Jahn-Teller distortion of Cu^{2+} can enhance the interstitialcy diffusion of oxide ion [32].

The electrical conduction of hole is observed in this type of compounds [32]. Thus, these materials are applicable to cathode, rather than electrolyte in cells (detailed explanation will be given in Section 1.3.1).

1.2.4 Anisotropic structures (1D, 2D, 3D path)

In this section, anisotropic structures having 1D, 2D, or 3D paths are briefly reviewed.

The 1D structure in ionic conductors is often called as tunnel structure. This structure has a tube-like framework and the conducting ions are located at inner core. One example is an apatite-type compound with general composition of $A_{10}(MO_4)_6O_2$ (A = alkaline earths or rare-earths, M = Si, Ge, P). This structure can be divided into $A_4(MO_4)_6$ framework, and A_6O_2 units located in the cavity of this framework [35].

A representative example of 2D path conductor is β-alumina ($Na_2O \cdot 11Al_2O_3$), where Al^{3+} and O^{2-} form the layered structure (spinel-type blocks), and Na^+ ion passes between these layers [36].

Ionic conductor with 3D path means the network structure, one example of which is NASICON ($Na_3Zr_2PSi_2O_{12}$) [37].

1.3 Social demands for ionic conductors

Ionic conductors are indispensable for electrolytes in fuel cells and secondary batteries, which are expected to be the next generation energy resources [38]-[40]. For example, in the automobile industry, the development of fuel cell vehicles or electric vehicles is one of hot issues.

As schematically illustrated in Fig. 1-9, both devices mainly consist of cathode, anode and electrolytes. In order to operate actual systems, many other components are necessary, such as interconnects, seals, and so on.

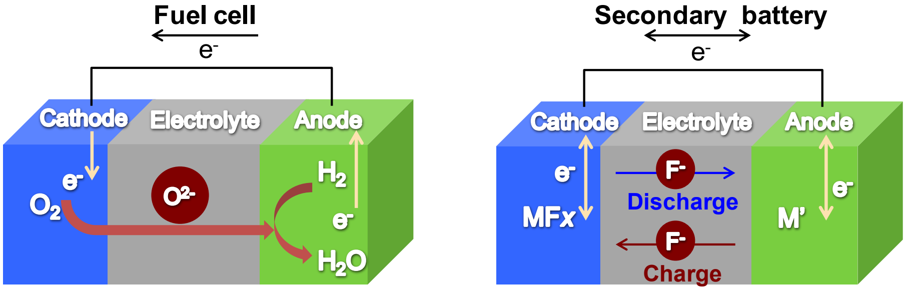

Fig. 1-9 Schematics of **(a)** fuel cell (ex. solid oxide fuel cells) and (b) secondary battery (ex. fluoride ion battery, described in Ref. [40]).

The electrolytes, transferring the ions between cathode and anode, play an important role for the performance of batteries. Thus, investigating high ionic conducting materials is a crucial demand for operating such resources. For such industrial demands, ionic conductors are the subjects of current intensive studies.

1.3.1 Electrolytes for fuel cells

Fuel cells can be classified by the conducting ionic species or working temperature, as listed in Ref. [38] and [41]. First, the general features of fuel cells are briefly mentioned. In these devices, the anode is called fuel electrode, into which fuel gasses such as H_2 are supplied. Such gasses sometimes need purification depending on the condition of devices (such as operation temperature). On the other hand, at the cathode, infinite resources such as air are used. In principles, one can extract the electricity from the air without releasing any harmful compounds. Thus, these devices are often called as clean energy resources.

In this section, the working mechanism and representative materials of fuel cells will be reviewed. Each kind of fuel cell has both advantages and disadvantages. It is necessary to adopt appropriate materials for each purpose and take technical points, apart from the ionic conductivity itself, into account. Details about the following fuel cell were described in Ref. [38] and [41].

Solid oxide fuel cell (SOFC)

SOFC is operated at the highest temperature (about 750–1000°C) among the fuel cell systems. It is used in our daily life as co-generation systems and SOFC vehicles, which is now under intensive development. SOFC has some advantages as all-solid fuel cells, for safety and convenience. Additionally, high operation temperature of SOFC contributes to save the expensive catalysts such as Pt. However, because of all-solid and high operation temperature, difference in thermal expansion coefficient causes a serious problem of cracking [38]. Consequently, there is a demand to reduce the operation temperature of SOFC (intermediate temperature (IT)-SOFC [38][31]). The size minimizing is another trend for recent SOFC application (μ-SOFC [42]).

The operation principle of SOFC is very simple as described by the following equations:

$$\text{Cathode: } O_2 + 4\,e^- \rightarrow 2\,O^{2-} \quad (1\text{-}6)$$

$$\text{Anode: } 2H_2 + 2O^{2-} \rightarrow 2H_2O + 4e^-. \quad (1\text{-}7)$$

From the overall reaction, only H_2O is produced. As is the same for other fuel cells, the triple phase boundary (TPB, Fig. 1-10) strongly affects the performance [38][43][44]. TPB is the boundary between electrode, electrolyte and supplied air. As can be seen in Fig. 1-10, both electronic and ionic current flow through the cathode material.

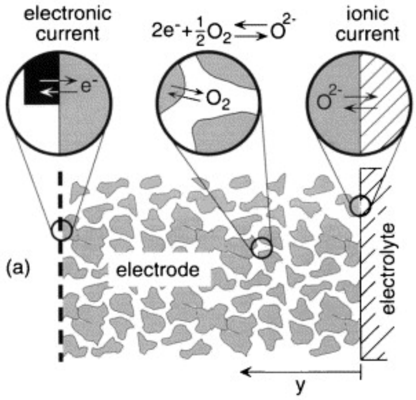

Fig. 1-10 Schematic of triple phase boundary (TPB). Reprinted with permission from [S.B. Adler, Solid State Ionics **111**, 125 (1998).], copyright Elsevier, 1998.

On the other hand, pure ionic conduction is required for electrolytes since the electronic current will cause short-circuit of the devices. The oxide ion conducting materials can be utilized either for cathode or electrolytes depending on its electronic conduction.

Molten carbonate fuel cell (MCFC)

The working temperature of MCFC is the second highest among the fuel cells, which is about 650°C. This relatively high working temperature saves the Pt catalyst as in SOFC case. This high temperature also makes it possible to save the cost for reforming gas, which is necessary for lower temperature fuel cells. MCFC can use CO_2 or CO as inflows other than O_2. The carbonate ion CO_3^{2-} passes the electrolyte as a carrier ion. Corrosion by molten carbonate is one of the problems in practical MCFC.

Phosphoric acid fuel cell (PAFC), Polymer electrolyte (membrane) fuel cell (PE(M)FC), and Alkaline fuel cell (AFC)

PAFC, PE(M)FC and AFC work at relatively low temperature, which requires pure H_2 supplied into anodes (i.e. requires external reformation of gas). Their carriers are H^+ for PAFC and PE(M)FC, and OH^- for AFC. PAFC is an already established device, and we can see numbers of co-generation systems installed around the world. However, there are few rooms to reduce the capital cost of this device, so the alternative devices, such as SOFC, MCFC, and PE(M)FC, is attracting more attention [41]. PE(M)FC is a representative fuel cell working at low temperature (about 200°C), which is applied to portable energy resources. CO-tolerance of anodes is one of the issues to be solved. AFC has an advantage that it can work at the lowest temperature (about 70°C). Due to the low temperature, however, high purification of gas is required, which strongly limits the application field of this device.

1.3.2 Electrolytes for secondary batteries

Secondary batteries have almost the same components as fuel cells. A main difference is the charge/discharge process. In fuel cells, the reaction proceeds as described in Eqs. (1-6) and (1-7), generating H_2O as a product. In secondary batteries, the conducting ions such as Li^+ are inserted into the electrodes, changing its position in charge/discharge process repeatedly.

In our recent daily life, Li ion-based secondary batteries are rapidly increasing their shares. On the one side, we can obtain convenience life by these developments. On the other side, however, they sometimes cause serious incidents, which are new to our memory, such as fire out of cellular phone or engine system of airplane [45][46]. These incidents remind us that operation of the system cannot always be obtained as expected in actual systems, so that we should keep our mind on preparing for the worst. Furthermore, it is important to select safer materials for applications. In the case of the incident about engine system of airplane, lithium salt in organic solvent was used as the electrolyte material. The volatility of this solution is suggested as one of the major safety issues with lithium ion batteries [45]. If alternative all-solid lithium ion batteries were used, such incidents might have been prevented though another drawback such as cracking might arise. At any rate, developments of alternative solid-state devices, not limited to lithium ion batteries, have an important meaning for applications. Lithium ion conductors, $Li_{2+2x}Zn_{1-x}GeO_4$ ($x = 0.55$), $Li_{3x}La_{2/3-x}TiO_3$ ($x = 0.167$) and LISICON, are promising materials towards all-solid Li ion batteries [37].

Recently, fluoride ion-based secondary battery has been investigated as another candidate of secondary battery [40][47]. In principle, construction of fluoride ion battery is possible by fabricating [metal (M)]/[fluoride ion conductor]/[metal fluoride ($M'F_x$)] structure. The suggested advantages of fluoride ion battery are its high theoretical voltages and high theoretical energy density [40]. Fluoride ion batteries are still in developing stage; their practical application to industrial products has not been achieved to date because of the low capacity compared to its theoretical value and decline during charge/discharge cycles [48][49]. Thus, exploration and improvement of fluoride ion conductors are strongly required not only from the fundamental scientific interest but also for the application purposes.

1.4 How to measure the ionic conductivity

1.4.1 Direct measurement and indirect measurement

In the previous section, I described the motivation for investigating ionic conductors. In this section, several methods to evaluate ionic conductivity are introduced. Ionic conductivity can be measured by direct (observing the motion of ions that obey Fick's law) or indirect techniques, as follows [11].

Direct measurement:

Secondary ion mass spectrometry (SIMS), electron microprobe analysis, Auger electron spectroscopy, spreading resistance profiling (for semiconductors)

Indirect measurement:

Impedance spectroscopy, Mössbauer spectroscopy, mechanical spectroscopy, nuclear magnetic relaxation, quasielastic neutron scattering

The diffusion of ions itself can be directly measured by observing tracer diffusion or chemical diffusion. The typical procedure to determine the ionic conductivity of solid-state materials is tracer diffusion using SIMS [50][51]. In the tracer diffusion technique, ions are labeled by tracer in the procedure such as annealing under $^{18}O_2$ gas atmosphere.

The most conventional technique to measure the ionic conduction is impedance spectroscopy [44][52]. Impedance is defined by

$$Z(j\omega) = u^*(t) / i^*(t) = (U / I) \exp (j(\varphi - \psi)) = |Z| \exp (j\theta) = Z_{Re} + j\, Z_{Im}, \qquad (1\text{-}8)$$

where $u^*(t) = U \exp(2\pi ft + \varphi)$ and $i^*(t) = I \exp(2\pi ft + \psi)$. $u(t) = \mathrm{Re}[u^*(t)]$ is the input voltage and $i(t) = \mathrm{Re}[i^*(t)]$ is the electric current in response (U, I: amplitude, φ, ψ: initial phase). The plot of $-Z_{Im}$ versus Z_{Re} will have semi-circle form so as to fulfill $\omega RC = 1$ (Fig. 1-11). This plot is called Cole-Cole plot, from which the resistance can be evaluated as a diameter of the circle.

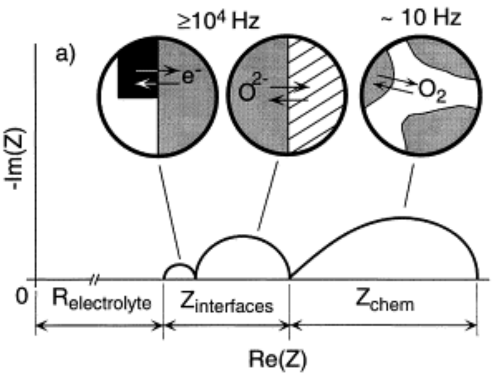

Fig. 1-11 Schematic of Cole-Cole plot measured in SOFC device. Reprinted with permission from [S.B. Adler, Solid State Ionics **111**, 125 (1998).], copyright Elsevier, 1998.

In Ref. [52], many studies on impedance measurement are reviewed. Ref. [53] compares the tracer diffusion coefficient D^* and conductivity-based diffusion coefficient D_σ converted from the conductivity σ by impedance spectroscopy. The ratio of D^*/D_σ is referred to as Haven ratio H_R, which is equal to the correlation factor f (described in Section 1.1.5) in simple cases. In the collective mechanisms, such as interstitialcy mechanism, the relations between H_R and f will be $H_R = f\, d^2/f_{\mathrm{AA}} d_q^{\,2}$, where d and d_q are the jump distances of tracer and charge, respectively [11].

Other methods have also been used to directly observe ionic motion, as follows; ^{19}F fast magic angle spinning nuclear magnetic resonance technique [28], quasielastic neutron scattering [54], and so on. Electron/nuclear density distributions and diffusion path can be visualized by analyzing synchrotron/neutron diffraction data with Rietveld technique and maximum-entropy-method (MEM)-based pattern fitting [32]. These studies often adopted complementary theoretical calculation [32][54].

1.4.2 Ionic conduction vs. electronic conduction

In the discussion of ionic conductors, we must consider the electric conduction of materials since the ionic conduction is often accompanied with electronic conduction.

In chemical compounds, there are several possible carriers such as hole $\mathrm{h}^{\cdot}$, electron e’, and ion. As can be inferred from the equilibrium state, for example in case of simple oxides MO, they will change depending on the partial oxygen pressure (P_{O2}) as follows:

$$(\text{low } P_{\mathrm{O2}}) \quad \mathrm{O_O^{\times}} = \mathrm{V_O^{\cdot\cdot}} + 1/2\ \mathrm{O_2} + 2\mathrm{e'}, \quad K = [\mathrm{V_O^{\cdot\cdot}}]\,[\mathrm{e'}]^2\, P_{\mathrm{O2}}^{\ 1/2} \tag{1-9}$$

$$(\text{high } P_{\mathrm{O2}}) \quad 1/2\ \mathrm{O_2} = \mathrm{V_M''} + \mathrm{O_O^{\times}} + 2\mathrm{h}^{\cdot}, \ K = [\mathrm{V_M''}]\,[\mathrm{h}^{\cdot}]^2\, P_{\mathrm{O2}}^{\ -1/2}. \tag{1-10}$$

The diagram of conducting species against the activity (such as a_{Li} or P_{O2}) is called Brouwer diagram, as schematically shown in Fig. 1-12 [55][56].

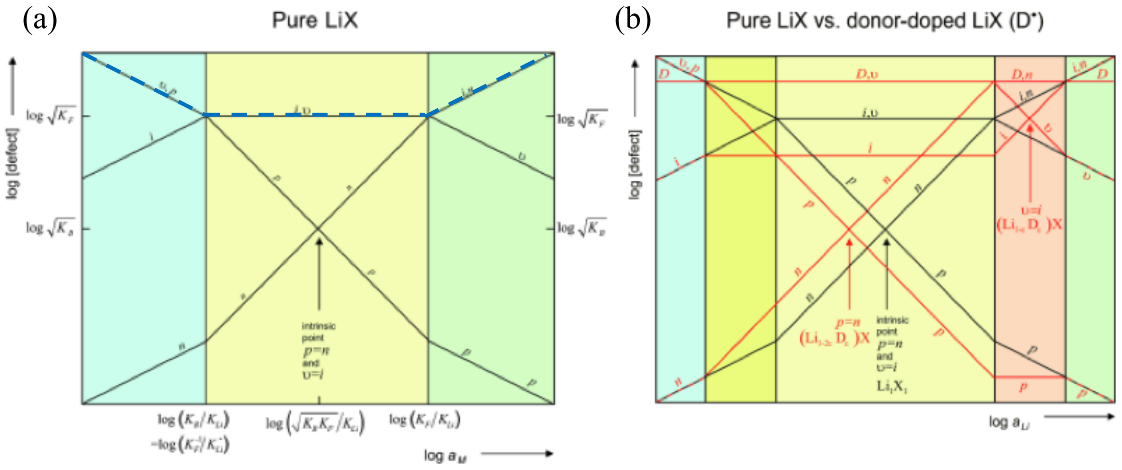
(a)
Pure LiX
log [defect]
log √K_F
log √K_s
i,υ
intrinsic point
p=n
and
υ=i
log a_M
(b)
Pure LiX vs. donor-doped LiX (D•)
log [defect]
log √K_F
log √K_s
D,υ
D,n
υ=i
p=n
Li_1X_1
log a_Li

Fig. 1-12 Brouwer diagram of conducting species (electron, hole, and ion); (a) pure material (b) doped material (donor-doped). Reprinted with permission from [J. Maier, Angew. Chem. Int. Ed. **52**, 4998 (2013).], Copyright © 2013 WILEY‐VCH Verlag GmbH & Co. KGaA, Weinheim.

The observed conductivity will be dominated by the most contributing conducting species (dashed blue line in Fig. 1-12(a)). Figure 1-13 provides the actual measurement of the conductivity versus activity (e.g. P_{O2}) plot [16], which will provide information about the major conducting species.

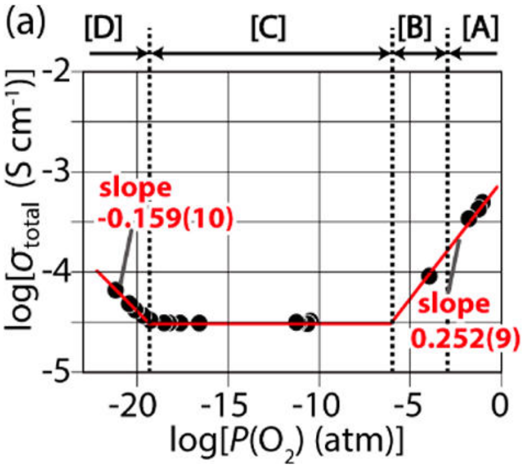

Fig. 1-13 Total conductivity against P_{O2} (the sample is $NdBaInO_4$ in Ref. [16]). Reprinted with permission from [K. Fujii, Y. Esaki, K. Omoto, M. Yashima, A. Hoshikawa, T. Ishigaki, and J. R. Hester, Chem. Mater. **26**, 2488 (2014).] Copyright 2014 American Chemical Society.

Each region in Fig. 1-13 represents the following feature; [A] hole conductor, [B] mixed oxide-ion and hole conductor, [C] pure oxide-ion conductor, and [D] electronic conductor. As already mentioned in Section 1.3, ionic conductors cannot be applied to the electrolytes of batteries if they show electronic conduction. The materials exhibiting both ionic and electronic conductivities can be used as the cathode of fuel cells. Consequently, the range of P_{O2} indicating pure ionic conduction (region [C] in Fig. 1-13) is important for stable operation as electrolytes of batteries. This P_{O2} range can be controlled by doping as in Fig. 1-12(b). Thus, doping has another potential to control the ionic conducting properties.

1.5 Advantages of theoretical calculation

As shown in Section 1.4.1, theoretical calculations are often combined with experimental measurement and give useful information about the ionic conduction mechanism [32][54]. The most common measurement, impedance spectroscopy, gives the net ‘result’ of conductivity, although it cannot provide any insight into microscopic ‘mechanism’ of the ionic conduction. Observation of conducting path is possible by the methods such as neutron and synchrotron methods [32][54], however, these measurements often require large-scale facilities.

Theoretical calculations can provide important information about ionic conduction mechanism; they can directly observe the motion of each ion in materials, estimate the migration barrier of ionic conduction, trace the electronic configuration, and so on. Detailed explanation about each calculation method will be given in Chapter 2. Preceding studies of theoretical calculations will be introduced in Chapter 3, 4 and 5.

1.6 Purpose of this study

Solid-state ionic conductors are widely used as ionic sensors and electrolytes for fuel cells and secondary batteries. The social demands for them are increasing day by day.

Fluorite structure is one of the most typical mother structures of ionic conductors. Fluorite compounds have the composition of MX_2, and sometimes compete with other polymorphs depending on the ratio of ionic radii (r_{cation}/r_{anion}) and/or ordering of ions.

In this thesis, I focused on two materials with fluorite structure, ZrO_2 and LaOF. From the first-principles simulations, ionic conduction mechanisms in fluorite structure were discussed in terms of the ionic radius and anion ordering. For the former viewpoint, the relation between ionic radius and cell volume of compounds could change by applying the strain. First, I investigated the mechanism of the enhanced ionic conduction in ZrO_2 systems under tensile strain, which was first reported by experiments (Chapter 3). Next, N and F anion doping into ZrO_2 was proposed as an alternative approach to the well-established cation doping (Chapter 4). Finally, I studied the ionic conduction in a mixed anion compound, LaOF (Chapter 5). The ionic conduction mechanism was discussed from the viewpoint of anion ordering.

Chapter 2 Calculation method

2.1 Concept of theoretical calculation

As mentioned in Section 1.5, theoretical calculations can provide important information about ionic conduction mechanism, which cannot or is difficult to be accessed directly by experimental measurements. By theoretical calculations, it is possible to directly observe the motion of each ion in materials, estimate the migration barrier of ionic conduction, and trace the electronic configuration. In this chapter, I briefly introduce the procedures of these calculation methods.

Theoretical calculations, including density functional theory (DFT) calculation as a representative approach, are progressing rapidly. The accuracy of the calculations is reaching to that of experimental results. Nevertheless, I would like to stress that such simulation cannot fully treat the actual systems since the number of atoms available in the simulation is generally limited to 10^4–10^6 [57], or 10^8 in recent achievement [58], which is much lower than the number scale of actual systems (of the scale of Avogadro's number). Consequently, some approximation or extraction of the actual systems is needed in the computational simulations. We should select the proper procedures to achieve the respective purpose.

2.2 Density functional theory (DFT)

DFT is the most conventional approach for the theoretical calculation, which is established in 1964 [59]. In the chemical description, what we have to solve is Schrödinger equation, which is approximated into Hatree-Fock equation for conventional solution:

$$(-\frac{1}{2}\nabla^2 + V_{ion}(\mathbf{r}))\psi_i(\mathbf{r}) + \sum_j \int d\mathbf{r}' \frac{|\psi_j(\mathbf{r}')|^2}{|\mathbf{r}-\mathbf{r}'|}\psi_i(\mathbf{r}) - \sum_j \delta_{\sigma_\mathrm{i}\sigma_\mathrm{j}} \int d\mathbf{r}' \frac{\psi_j^*(\mathbf{r}')\psi_i(\mathbf{r}')}{|\mathbf{r}-\mathbf{r}'|}\psi_j(\mathbf{r}) = \epsilon_i\psi_i(\mathbf{r}). \quad (2\text{-}1)$$

In DFT, this Eq. (2-1) is converted into the problem of ‘electron density’ by using Hohenberg-Kohn-Sham theory [59][60]. The converted equation is called Kohn-Sham equation, which is described by $E[n(\boldsymbol{r})]$ (E: ground-state energy, $n(\boldsymbol{r})$: electron density at position $\boldsymbol{r}$). Because the energy E is the function of $n(\boldsymbol{r})$, which is the function of $\boldsymbol{r}$, this procedure is called density ‘functional’ theory. In Kohn-Sham equation, this $E[n(\boldsymbol{r})]$ is decomposed into several parts: kinetic energy, Coulomb energy, contribution from external potential, and exchange correlation. The exchange correlation, described as $E^{xc}[n(\boldsymbol{r})]$, is unknown functional so that some approximation is necessary to solve the equation [61].

2.2.1 Functional

As shown above, the description of exchange correlation functional $E^{xc}[n(\boldsymbol{r})]$ is the important point in the DFT approach [61][62]. The simplest description is using constant value as in local density approximation (LDA), which was developed earlier:

$$E^{xc}[n(\overrightarrow{r})] = \int n(\overrightarrow{r})\epsilon_{xc}[n(\overrightarrow{r})]d^3r. \quad (2\text{-}2)$$

After that, the contribution of spin was taken into consideration, yielding local spin density approximation (LSDA):

$$E^{xc}[n(\overrightarrow{r})] = \int \epsilon_{xc}(n_\uparrow, n_\downarrow)n(\overrightarrow{r})d^3r. \quad (2\text{-}3)$$

From 1990s, the generalized gradient approximation (GGA) was adopted:

$$E^{xc}[n(\overrightarrow{r})] = \int \epsilon_{xc}(n_\uparrow, n_\downarrow, \overrightarrow{\nabla} n_\uparrow, \overrightarrow{\nabla} n_\downarrow)n(\overrightarrow{r})d^3r. \quad (2\text{-}4)$$

Including a Hubbard correction as the GGA+U method, the electronic description is further improved. This approach is often applied in description of the electronic configuration in transitional metal compounds.

In recent approaches, hybrid functional mixing the exchange integral of

Hatree-Fock was also adopted as follows [62]:

$$E^{xc}[n] = \int_0^1 U_\lambda^{xc}[n]d\lambda \sim \frac{1}{2}U_0^{xc}[n] + \frac{1}{2}U_1^{xc}[n]\ , \tag{2-5}$$

where U_0^{xc}, U_1^{xc} corresponds to the nonlocal exchange energy of Kohn-Sham orbitals, potential energy for exchange and correlation, respectively. This procedure is implemented in Heyd–Scuseria–Ernzerhof (HSE) functional, which is more accurate but high-cost [63][64].

Until now, many other functional are provided such as Wu-Cohen (WC) functional [65]. In the present study, I adopted GGA level of theory with the Perdew-Burke-Ernzerhof (PBE) functional [66]. For comparison, HSE functional and WC functional were partly adopted (see Chapter 5).

2.2.2 Pseudo potential, wavefunction

In DFT calculation, only valence electrons were treated for solving the Kohn-Sham equation. The core electrons were rewritten for simple description so as to be easily solved. This potential is called pseudo potential [61]. In the present calculations, the projector-augmented wavefunction (PAW) approach was used to treat the effect of the core electrons [67]. In the calculations of this study, the employed PAW data sets treated the $5s^2 4d^2$ orbital in Zr, $5s^2 5p^6 5d^1 6s^2$ electrons in La, $2s^2 2p^4$ orbital in O, $2s^2 2p^3$ orbital in N, and $2s^2 2p^5$ orbital in F as the valence orbitals. The Kohn–Sham orbitals for the valence electrons were solved as linear combination of a plane-wave basis set with an energy cutoff of specified values.

2.2.3 *K*-points

K-point is a grid of simulated cell. Calculation at many mesh points is more accurate but its computational cost is high. In the present study, Monkhorst-Pack *k*-point mesh was adopted with the selected grid regarding to the respective cell size [68].

2.2.4 Simulation package VASP

Vienna *ab initio* Simulation Package (VASP) is well-established software to implement DFT calculations [69]. In the present study, I used this software for optimization of the structure, and *ab initio* MD simulation.

2.3 Density functional perturbation theory (DFPT)

2.3.1 Phonon calculation

In the density functional perturbation theory (DFPT), the second and third derivatives of the total energy are calculated, providing phonon dispersions [70]. In the phonon calculation, the grid is referred to as '*q*'-points instead of *k*-points. Phonon calculation can find the dynamical instability of the structure. In usual optimization, one cannot find its instability if the structure is just at the top of the potential energy. The procedures of the optimization using phonon calculation are described as follows. First, phonon dispersion curves are drawn connecting the high symmetry *k*-points in the cell. The imaginary frequencies (i.e. negative values) correspond to the dynamical instability of the structure. The positions of atoms are displaced along the eigenvector for the dynamical matrices with the largest negative frequency. The resulting structure is optimized in the usual procedure. This procedure was repeated until no imaginary phonons appeared, i.e., dynamical instability was completely eliminated. Hereafter, the stable structure with no negative eigenvalue in the corresponding dynamic matrix is referred to as the "dynamically stable" structure [71]. For the results of phonon calculations in this study, see Section 3.3.1.

2.3.2 Simulation package QE

In the present study, Quantum ESPRESSO (QE) package was used for phonon calculation [70]. This simulation package can also conduct the usual optimization of the structure. QE software supplies various pseudo potentials and functionals in the database. Though the usual optimization was basically conducted by the conventional simulation package VASP, QE software was additionally used to compare the result of calculation using other functional (for the results, see Section 5.3.1).

2.4 Formation energy of Frenkel pair

In this section, the evaluation of formation energy of Frenkel pair is described. Generally, the formation energy of an isolated defect D in charge state q can be calculated by the standard equation [72]:

$$\Delta H_{D,q}(E_F,\mu) = [E_{D,q} - E_H] - q(E_V + \Delta E_F + \delta E_V) + \Sigma n_\alpha(\mu_\alpha^0 + \Delta\mu_\alpha)\ , \tag{2-6}$$

where $E_{D,q}$ is the total energy of model cell with defect and additional q electrons ($q > 0$ for negatively charged state), E_H is the total energy of pristine model cell (= host), E_V is the Kohn–Sham energy level of valence band in the model cell with defect, n_α is the number of subtracted atoms ($n > 0$ for removal of atoms from system to environment). δE_V is the origin of electronic static potential in defect cell relative to that in pristine model cell. The formation energy has two parameters; E_F is the Fermi level of the system, μ_α is the chemical potential of component α.

Decomposing the Frenkel pair into vacancy and interstitial (for example, $\mathrm{F_F^{\times}} \rightarrow \mathrm{V_F^{\bullet}} + \mathrm{F_i^{'}}$ or $\mathrm{O_O^{\times}} \rightarrow \mathrm{V_O^{\bullet\bullet}} + \mathrm{O_i^{''}}$), the formation energy of vacancy ($\mathrm{V_F^{\bullet}}$ or $\mathrm{V_O^{\bullet\bullet}}$) and interstitial ($\mathrm{F_i^{'}}$ or $\mathrm{O_i^{''}}$) can be written as follows:

$$\Delta H_{\mathrm{vac},q}(E_F,\mu) = [E_{\mathrm{vac},q} - E_H] + q(E_V + \Delta E_F + \delta E_V) + \Sigma n_\alpha(\mu_\alpha^0 + \Delta\mu_\alpha) \quad \text{(2-7)}$$

$$\Delta H_{\mathrm{int},q}(E'_F,\mu) = [E_{\mathrm{int},q} - E_H] - q(E'_V + \Delta E'_F + \delta E'_V) - \Sigma n_\alpha(\mu_\alpha^0 + \Delta\mu_\alpha). \quad \text{(2-8)}$$

Under the condition that vacancy and interstitial have the same Fermi level (measured from the electrostatic origin of the pristine cell; $E_V + \Delta E_F + \delta E_V = E'_V + \Delta E'_F + \delta E'_V$), the summation of $\Delta H_{vac,q}$ and $\Delta H_{int,q}$ should give the formation energy of infinitely separated Frenkel pair:

$$\Delta H_{\mathrm{Frenkelpair}} = \Delta H_{\mathrm{vac},q}(E_F,\mu) + \Delta H_{\mathrm{int},q}(E_F,\mu) = (E_{\mathrm{vac},q} - E_H) + (E_{\mathrm{int},q} - E_H). \quad \text{(2-9)}$$

Alternatively, the formation energy of Frenkel pair was calculated using large extended unit cells as follows:

$$\Delta H_{\mathrm{Frenkelpair}} = E_{\mathrm{Frenkelpair}} - E_H\,. \quad \text{(2-10)}$$

The coincidence of the values calculated from Eqs. (2-9) and (2-10) indicates that a satisfactorily large unit cell is used in the calculation.

2.5 Molecular Dynamics (MD) simulation

Molecular dynamics (MD) simulation is a powerful tool to trace the motion of ions in ionic conducting materials. In actual ionic conductor, ionic motion is driven by concentration gradient of ion (e.g. electrolytes of fuel cells, gas sensors) or the external electric field (e.g. electrolytes of secondary batteries during charging process). Though MD simulations only trace the motion of ions at finite temperature, diffusion coefficient D can be obtained from such ionic motion, which is related to ionic conductivity σ by Nernst-Einstein equation (see Section 2.6.2). Since theoretical simulations including concentration gradient and/or external electric fields are difficult, such MD simulation at finite temperature is the most conventional approach to discuss the ionic conducting properties.

There are several kinds of MD simulations. Among them, classical MD and *ab* *initio* MD simulation are two of the most conventional approaches.

2.5.1 Classical MD simulation

In classical MD simulation, the empirical potentials, based on the two-body approximation, are used. It does not solve the electron density as described in Section 2.2, but optimizing the parameter describing the atomic species in advance [73]. This approach permits the use of large unit cells and long simulation times. However, the obtained results are not always reliable compared to those of *ab initio* MD simulations described below.

2.5.2 *Ab initio* MD simulation

Among the MD simulations, *ab initio* MD simulation should be the most reliable since it solves the electron density at each simulation step, based on DFT. However, the feasible unit cell sizes and simulation times have been limited because of the computational cost. The cell size of simulation is generally limited to several hundreds of atoms, and the simulation time is limited to several to several tens picoseconds or so. In this study, I adopted this *ab initio* MD simulation to describe the ionic conduction.

In *ab initio* MD simulation**,** the dynamics of ions were calculated based on the Hellmann‐Feynman force acting on the atoms. A Nóse–Hover thermostat was used to control the temperature. In this study, I gradually raised the temperature in MD simulation. A gradual structural transformation was observed with increasing temperature, ensuring that the present calculation described the appropriate motion of the ions at finite temperatures. This gradual change in temperature caused the relevant structural relaxation from the initial thermodynamically-unstable structure. This preliminary step may contribute to eliminate the dependency on the initial guess of the structure.

2.6 Evaluation of the ionic conductivity

2.6.1 Mean square displacement (MSD)

Generally, the ionic conductivity is evaluated as the mean square displacement (MSD) given by the following equation, using the data of trajectories in MD simulations:

$$\mathrm{MSD}(t) = \frac{1}{n}\sum_{ri} \mid r_i(t) - r_i(0) \mid^2 = 6Dt + \mathrm{const.} \tag{2-11}$$

where D is the diffusion coefficient, n is the number of particles, and $r_i\,(t)$ is the position of ion i at time t. The MSD was then smoothed by averaging MSD (t, t_0) over the time origin t_0 in order to estimate the diffusion coefficient:

$$\mathrm{MSD}(t, t_0) = \frac{1}{n}\sum_{ri} \mid r_i(t + t_0) - r_i(t_0) \mid^2. \tag{2-12}$$

The results from Eqs. (2-11) and (2-12) should coincide at the thermodynamical limit ($n \rightarrow \infty$, $t \rightarrow \infty$).

2.6.2 Nernst–Einstein relation

The ionic conductivity σ, observed experimentally, is related to the diffusion coefficient D (namely, charge diffusion coefficient D_σ) through the Nernst-Einstein relation:

$$\sigma = Nq^2 D_\sigma / k_\mathrm{B} T, \tag{2-13}$$

where N and q are the density and the charge of the mobile ions, respectively. For example, if $\mathrm{V_O^{\cdot\cdot}}$ or $\mathrm{O^{2-}}$ carries charges, a nominal charge of ±2 is contributing to the conduction.

The diffusion coefficient D is theoretically obtained as the product of the migration energy of individual carrier and the concentration of carriers C_s, which is temperature dependent [74]. The concentration of Frenkel pair can be estimated by Eq. (1-1) in Section 1.1.2:

$$Cs = \sqrt{}\,(NN') \exp\left(-W_F/2k_BT\right)/N_A. \tag{1-1}$$

The Nernst-Einstein relation in Eq. (2-13) can be described using Cs as follows:

$$D_\sigma = RT\sigma/(m^2CsF^2), \tag{2-14}$$

where the variable m is effective number of electrical charges by carrier, F is Faraday constant [75]. The diffusion coefficient D obtained by MD calculation is consistent with D_σ when correlation factor f is consistent with Haven ratio H_R (see Section 1.4.1). The activation barrier E_a is derived from the temperature dependence of D, which is proportional to exp ($-E_a/k_BT$). Using these relations, the calculated results can be compared to the corresponding experimental data (will be discussed in Chapter 5).

2.7 Evaluation of the bonding character

2.7.1 Electronic density distribution

The DFT calculations of solid-state compounds assuming periodic boundary conditions primarily solve the electron density. Thus, the electron density distribution is traceable during the migration of ions, which permits to discuss the mechanism of ionic conduction as in Ref. [32] and [76].

2.7.2 Crystal Orbital Hamilton Population (COHP)

As shown in the previous section, some properties such as electron density distribution are obtained as a result of DFT calculation, which assist the argument on the ionic conduction mechanism. From the viewpoint of chemistry, bonding character would be essential to understand the properties of compounds [77]. Crystal Orbital Overlap Population (COOP) or Crystal Orbital Hamilton Population (COHP) is a powerful tool to calculate such characters [78]-[81]. This approach has an advantage to directly and concretely discuss the strength of certain bonds.

The concept of COOP is first developed using tight-binding extended Hückel calculations. The COOP was defined by Hughbanks and Hoffmann in 1983 by the following equation [77];

$$\mathrm{COOP}_{\mu\vec{T},\nu\vec{T'}}(E) = S_{\mu\vec{T},\nu\vec{T'}} \sum_{j,\vec{k}} {C^*}_{\mu\vec{T},j}(\vec{k})\, C_{\mu\vec{T'},j}(\vec{k})\, \delta(\epsilon_j(\vec{k}) - E), \tag{2-15}$$

where $C(\boldsymbol{k})$ contains the coefficients of linear combinations of atomic orbitals μ to represent crystal orbitals. Since the COOP method requires electron number partitioning using localized orbitals, its application to first principles DFT calculation using plane wave is difficult. It is much easier to use energy-resolved bonding descriptor; this approach was introduced in 1993 as COHP analysis. COHP uses Hamiltonian matrix rather than overlap matrix [78];

$$\mathrm{COHP}_{\mu\vec{T},\nu\vec{T'}}(E) = H_{\mu\vec{T},\nu\vec{T'}} \sum_{j,\vec{k}} f_j(\vec{k})\, {C^*}_{\mu\vec{T},j}(\vec{k})\, C_{\mu\vec{T'},j}(\vec{k})\, \delta(\epsilon_j(\vec{k}) - E), \tag{2-16}$$

where H is the elements of Hamiltonian matrix $\boldsymbol{H}$, and $f_j(\boldsymbol{k})$ are the occupation numbers. Basically, COHP analysis also requires local basis. On the contrary, the configuration by PAW approach implemented in the software such as VASP is delocalized one. In order to fill this gap, the projector scheme is applied.

In PAW approach, the band wavefunction $|\psi_j(\boldsymbol{k})>$ is expressed through a pseudospace function and an additional "augmentation part". In order to analyze, this PAW should be converted into local function and its combination. In the procedure of projection, one needs to choose local orbitals and to transform them to reciprocal space.

In principle, the choice of basis is arbitrary, as long as the latter is able to represent the PAW function and allows for chemical interpretation. A reasonable basis is contracted primitive Slater-type orbitals. Finally, we can obtain the projected COHP values as a product. All the procedure described above is already established in the software LOBSTER as described below.

2.7.3 Simulation package LOBSTER

In the present study, COHP analysis was adopted as implemented in LOBSTER package [78]-[81]. The obtained COHP result is just as an extension of density of states (DOS) plot having positive/negative values for anti-bonding/bonding states, respectively. The integrated COHP up to the Fermi level (ICOHP) is a good indicator for comparing the bonding strength, where large negative ICOHP values correspond to strong bonding.

2.8 Evaluation of the migration barrier

2.8.1 Nudged elastic band (NEB) method

Nudged elastic band (NEB) method is used for evaluating the migration barrier of each migration mechanism. In NEB method, the initial and final structures were first set with linearly interpolated transition states. During the optimization of NEB method, these structures were treated as if they are connected with ‘elastic band’. This helps to search the minimum energy path for migration process without dropping off into the most stable state (i.e. not to avoid the saddle point in transition state). Climbing image (CI)-NEB method is a useful procedure to find the saddle point in a potential surface with smaller intermediate points [82][83]. In the present calculation, I adopted CI-NEB method with three intermediate images as implemented in VASP transition state tools (VTST) as follows.

2.8.2 VASP transition state tools (VTST)

VASP transition state tools (VTST) provide the tools for calculating migration barrier including CI-NEB [84]. In the CI-NEB calculations, I adopted VASP software combined with VTST.

Chapter 3 Phonon calculation and *ab initio* MD simulation of ZrO_2 systems under epitaxial strain

3.1 Introduction

As mentioned in Chapter 1, oxide ion conductors are attracting much attention as electrolytes for SOFC. In this chapter, I will discuss the oxide ion conduction of zirconia (ZrO_2)-based materials, which is one of the most conventional materials as oxide ion conductors. As in Section 1.2.1, ZrO_2 has three polymorphs: monoclinic ($P2_1/c$, <1400 K), tetragonal ($P4_2/nmc$, 1400–2600 K), and cubic ($Fm\bar{3}m$, >2600 K) phases [18]. The phase stability can be sensitively adjusted by varying the concentration of oxygen vacancies and/or the ratio of the ionic radii between the anion and the cation, both of which can be manipulated by substitution of aliovalent ions. Yttria stabilized zirconia ($(ZrO_2)_{1-x}(Y_2O_3)_x$, YSZ) has been widely used as a conventional electrolyte for SOFCs, but it requires high operation temperatures above 700 °C, which is one of the main drawbacks of YSZ with respect to practical applications.

---

*This chapter contains the contents of the following publications.

"DFT-based *ab initio* MD simulation of the ionic conduction in doped ZrO_2 systems under epitaxial strain"

M. Oka, H. Kamisaka, T. Fukumura, and T. Hasegawa, Phys. Chem. Chem. Phys. **17**, 29057 (2015).

© the PCCP Owner Societies 2015

Recently, multilayer thin films have been intensively studied because of their potential to exhibit higher ionic conductivities [50][85][86]. In 2008, Garcia *et al.* reported the in-plane 100-million-times-enhanced colossal ionic conductivity in a $(ZrO_2)_{0.92}(Y_2O_3)_{0.08}$ (8YSZ) and strontiumtitanate ($SrTiO_3$) heteroepitaxial structure [87]. Many studies have since been performed to elucidate the microscopic mechanism for this colossal ionic conductivity, but the origin of the observed high conductivity remains a controversial issue [88]-[90]. There is some argument over the origins of ionic conductivity. Fabbri *et al.* and Korte *et al.* reviewed the origin of ionic conductivity enhancement at the interface by examining two factors: space charge effect and epitaxial strain [91][92]. If the heterostructure is composed of intrinsic ionic conductors (Section 1.1.2), such as CaF_2/BaF_2 [85], the induced space charge region will significantly affect the ionic conductivity. On the other hand, in extrinsic ionic conductors, such as YSZ, the width of the space charge region is too narrow to affect the ionic conductivity, as it is inversely proportional to the square root of the concentration of the point defects. Therefore, the main contribution to the enhancement of ionic conduction in extrinsic ionic conductors will be the epitaxial strain at the interface [91][92]. Korte *et al.* classified the experimental data from literature, and categorized the YSZ/$SrTiO_3$ interface to be strain-controlled. From their theoretical analysis, Korte *et al.* argued that the increase in the ionic conductivity on the YSZ/$SrTiO_3$ interface would not exceed 10-fold [92]. Other studies ascribed the origin of the colossal ionic conductivity to a misidentification of the p-type electric conductivity in the $SrTiO_3$ substrate [88][89]. Thus, it is still unclear how large the increase of ionic conductivity in YSZ/$SrTiO_3$ system would be, whose typical values are limited to several to ten times in similar systems.

Several theoretical studies have attempted to clarify the role of the strain imposed at the interface of YSZ/$SrTiO_3$. Dezanneau *et al.* performed classical MD simulations in a 6 × 6 × 6 unit cell with randomly distributed Y dopants and oxygen vacancies [93]. The ionic conductivity reached a maximum at approximately 2–3% tensile strain along the *a*- and *b*-axes as observed in their results. *Ab initio* MD simulations by Pennycook *et al.* and Li *et al.* indicated the enhanced ionic conductivity at 7–10% tensile strain along the *a*- and *b*-axes [94][95]. Additionally, Li *et al.* took into consideration the interface effect, which can enhance the ionic conductivity to some extent [95]. However, Li *et al.* concluded that the interface does not produce a prominent increase in the ionic conduction. Generally, their *ab initio* MD simulations should be more reliable than the classical MD results. Due to the computational cost, however, they employed *cubic* undoped ZrO_2 with only one oxygen vacancy (V_O) within a 3 × 3 × 2 unit cell [94][95]. Pennycook *et al.* suggested the emergence of 'zigzag structure' of ZrO_2 by strain at low temperature, which breaks down to ionic conducting random structure at 2000 K [94]. Since they ignored the interaction of dopants or vacancies despite the difference in crystallographic symmetry between YSZ and ZrO_2 at room temperature, it is questionable whether such structural change or the ionic conduction of ZrO_2 can be applied to YSZ in actual system.

In this study, DFT-based *ab initio* MD simulations were performed to investigate how the ionic conduction in ZrO_2 systems is affected by three factors: strain, vacancies, and dopants. First, the most stable structure under tensile strain along the *a*- and *b*-axes was determined using DFPT-based phonon calculations, which was found to be completely different from the cubic structure. Second, finite temperature *ab initio* MD simulations were performed using the most stable structure under tensile strain as the initial structure. Notably, a number of oxygen vacancies deformed the spatial oxygen ordering state, which led to the enhancement of the oxide ion conductivity. The present results indicate that the oxide ion conductivity in ZrO_2 is largely influenced by the oxygen ordering pattern, which sensitively changes with the lattice strain and the number of cation dopants or oxygen vacancies.

3.2 Calculation method

First, the most stable structure of undoped ZrO_2 under 7% tensile strain along the *a*- and *b*-axes was determined using DFPT-based phonon calculations (Section 2.3). The atomic positions, lattice constants, and shapes of the primitive unit cell of ZrO_2 were obtained using the conventional structural optimization procedure as implemented in VASP (Section 2.2.4). In this optimization, the GGA-PBE functional was adopted with energy cutoff of 520 eV and the *k*-points of a 12 × 12 × 12 Monkhorst-Pack *k*-point mesh. In the case of non-doped cubic ZrO_2 with no oxygen vacancies, normal optimization terminated without causing any structural changes. The discrepancy in the calculated and experimental lattice constants for YSZ was approximately 1.2%, which is sufficiently small compared to the epitaxial strain at the YSZ/$SrTiO_3$ interface. The optimized cell was expanded along the *a*- and *b*-axes to match the lattice constant for $SrTiO_3$ with a 45° rotation (5.5225 Å), and thus reproduce the epitaxial strain in the YSZ/$SrTiO_3$ multilayer.

Phonon calculations were performed on the primitive cell using the QE package (Section 2.3.2). The *k*- and *q*-points were sampled with a 5 × 5 × 5 mesh. Phonon dispersion curves were drawn connecting the high symmetry *k*-points in the conventional cell [96]. The space group symmetry of the cell was identified using the spglib library [97]. The positions of the atoms were displaced along the eigenvector for the dynamical matrices with the largest negative frequency. The resulting structure was again optimized using VASP. This procedure was repeated until no imaginary phonons appeared, i.e., dynamical instability was completely eliminated. Phonon calculations for unstrained ZrO_2 were also performed, and the results agreed with those reported by

Parlinski *et al.* and Kuwabara *et al.* [98]-[100]. The space group of the dynamically stable structure without strain was determined to be $P4_2/nmc$ (0.03 eV/formula unit (eV/f.u.) stable from the cubic structure).

Next, *ab initio* MD simulations were conducted at finite temperatures starting from this dynamically stable structure. The system was first constructed using a periodic 3 × 3 × 2 supercell of undoped ZrO_2 with the dynamically stable structure as aforementioned. Three models were then constructed with different defect concentrations: a 3 × 3 × 2 unit cell of zirconia with (1) $1V_O$ ($Zr_{72}O_{143}\square$, where $\square$ denotes V_O); (2) $6V_O$ and no Y dopant ($Zr_{72}O_{138}\square_6$, $ZrO_{1.92}$); (3) $6V_O$ and compensating Y^{3+} ions ($Zr_{60}Y_{12}O_{138}\square_6$, $Zr_{0.83}Y_{0.17}O_{1.92}$, or $(ZrO_2)_{0.91}(Y_2O_3)_{0.09}$). The number of total electrons was adjusted to maintain the formal charge state for each ion. The charge neutrality of the cell was fulfilled by adding a compensating background charge. The *c*-axis length was optimized under the condition that the lengths of the *a*- and *b*-axes were fixed to those of $\sqrt{2} \times \sqrt{2}$ $SrTiO_3$. The stable structures of these supercells with some defects were obtained via normal structure optimization using VASP and a 2 × 2 × 2 *k*-point mesh with a cutoff energy of 520 eV. This structure was used as the initial structure for the *ab initio* MD simulations. The finite-temperature DFT-based *ab initio* MD simulations were performed using the PAW database. For the *ab initio* MD simulations, a softer pseudopotential for oxygen with a cutoff energy of 283 eV (=20.8 Ry) was selected. Only the Γ-point was sampled in the BZ. The lattice constants were fixed throughout the duration of the entire simulation. The time step for the MD simulation was 2.0 fs. The temperature was gradually increased from 500 to 2000 K during the first 1000 steps (t = 0–2 ps) and then held constant at T = 2000 K for the successive 4000 steps (t = 2–10 ps).

The ionic conductivity was evaluated as the MSD described as Eq. (2-11) in Section 2.6.1. The MSD was smoothed by averaging MSD (t, t_0) over the time origin t_0

(Eq. (2-12)). In the present study, the diffusion coefficient D was estimated by linear fitting of the MSD calculated from Eq. (2-12) using the data in the constant temperature region at $T = 2000$ K ($t = 2$–10 ps).

3.3 Results and discussion

3.3.1 Phonon calculations for undoped ZrO_2 under tensile strain

Figure 3-1(a) and (b) shows the phonon dispersion curves and the lattice structure of the cubic ZrO_2 cell under 7% tensile strain along the *a*- and *b*-axes (*I4/mmm*).

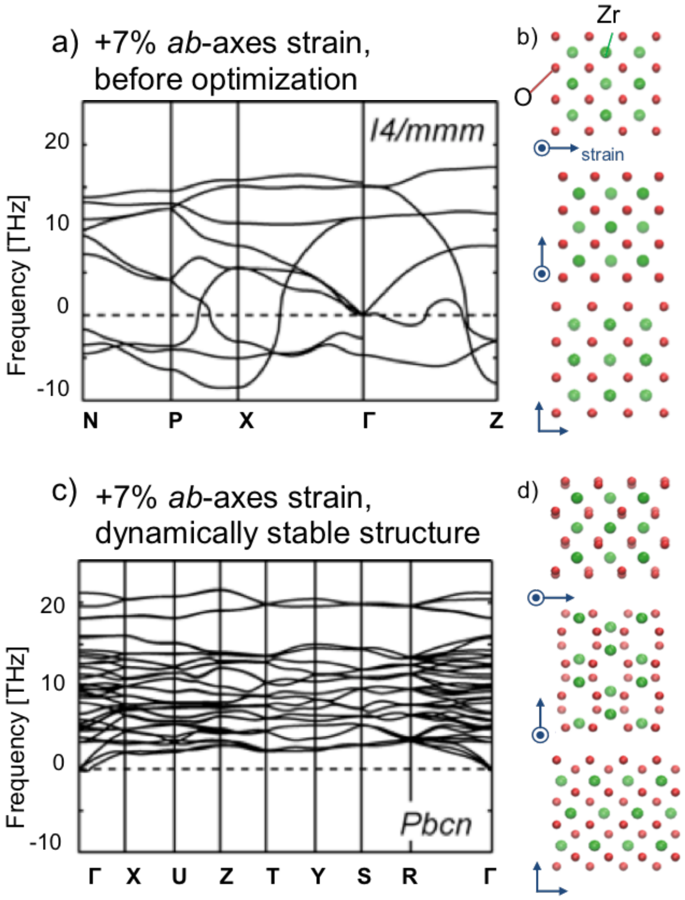

Fig. 3-1 (a) Phonon dispersion curves and (b) lattice structure for the cubic ZrO_2 cell under 7% *a,b*-axes tensile strain (*I4/mmm*). (c) Phonon dispersion curves and (d) lattice structure after optimization using phonon calculations.

Figure 3-1(a) reveals many imaginary frequencies expressed as negative values in the dispersion curves. These imaginary frequency phonons were successfully removed by the optimization with phonon calculation as shown in Fig. 3-1(c). Figure 3-1(d) presents the structure after removing the imaginary frequencies. This dynamically stable cell contains 12 atoms in a unit cell with the space group *Pbcn*. This structure is the same as the zigzag structure in previous study, which was suggested by the trajectory of MD simulation [94]. In this time, I precisely determined this structure by phonon calculation without any arbitrary process. Table 3-1 lists the space group symmetries and Wyckoff notations for the atomic positions in this structure (Fig. 3-1(d), *Pbcn*) and those in the initial structure (Fig. 3-1(b), *I4/mmm*).

Table 3-1 Space groups and Wyckoff notations for the optimized structure under 7% *a,b*-axes tensile strain.

atom	Wyckoff	*x*	*y*	*z*
I4/mmm (*before optimization*, *Fig. 3-1b*) ; *a* = 3.9050, *c* = 5.1390 [Å]				
Zr	*2a*	0	0	0
O	*4d*	0.500	0	0.250
Pbcn (*no imaginary frequency, Fig. 3-1d*) ; *a* = 5.1390, *b* = 5.5225, *c* = 5.5225 [Å]				
Zr	*4c*	0	0.679	0.250
O	*8d*	0.219	0.390	0.426

(Upper: the initial structure, bottom: the optimized structure using phonon calculations.)

The total energy decreased by 0.61 eV/f.u. after optimization of the phonons (i.e. from *I4/mmm* structure to *Pbcn* structure). This result suggests that cubic ZrO_2 under tensile strain (*I4/mmm*) is not an appropriate model cell and that the model cell should be built from this dynamically stable cell.

3.3.2 *Ab initio* MD simulations

Ab initio MD simulations were performed initiating from the dynamically stable structure described above. Three models were constructed using the procedure described in the Methods section: (1) $Zr_{72}O_{143}\square$, (2) $Zr_{72}O_{138}\square_6$, and (3) $Zr_{60}Y_{12}O_{138}\square_6$. Figure 3-2(a) and (b) compares the MSD values for the oxide ions calculated according to Eq. (2-11) using the data for t = 0–10 ps with and without 7% tensile strain along the *a*- and *b*-axes, respectively.

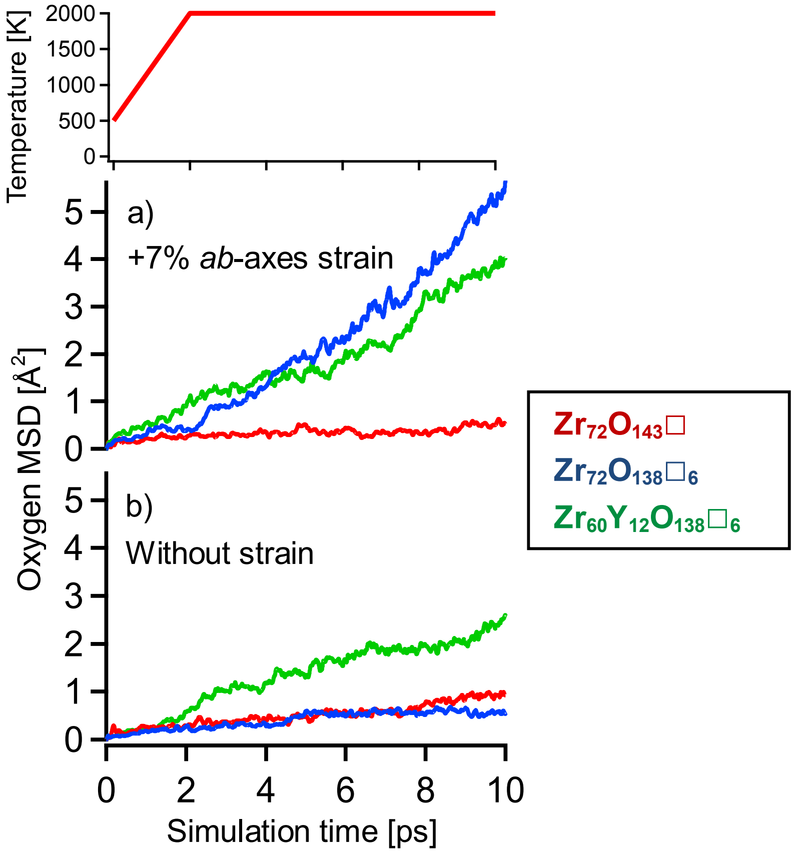

Fig. 3-2 MSDs of oxide ions in (red lines) $Zr_{72}O_{143}\square$, (blue lines) $Zr_{72}O_{138}\square_6$, and (green lines) $Zr_{60}Y_{12}O_{138}\square_6$ (a) with and (b) without 7% *a*,*b*-axes tensile strain. The temperature was controlled using the Nóse–Hover thermostat described as a temperature diagram. The MSD was calculated using Eq. (2-11), described in Section 2.6.1.

The statistics for the MSD were improved when the results from different initial times were averaged using Eq. (2-12) (Fig. 3-3). Since the linearity of the MSD over time was not analytically fulfilled at $t \rightarrow 0$, and the available sampling points in Eq. (2-12) became less frequent at longer t for the simulation with a finite time period, diffusion coefficients were calculated from the linear behavior between 0.3 ps and 7 ps in Fig. 3-3.

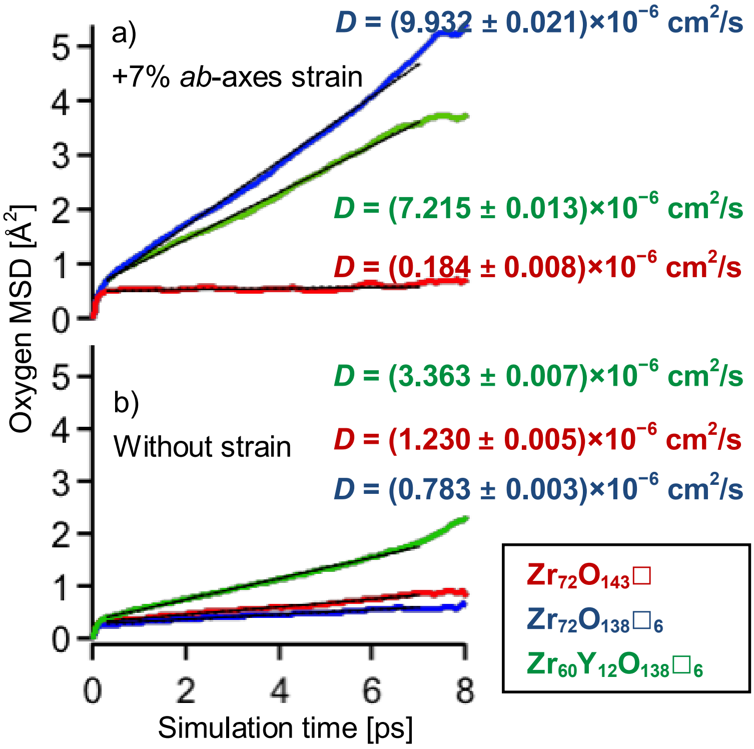

Fig. 3-3 MSDs of oxide ions at the constant temperature of 2000 K. The MSD was calculated from 2–10 ps of Fig. 3-2 using Eq. (2-12). Diffusion constants were calculated from linear behavior during 0.3 ps to 7 ps.

Unlike the previous studies [94][95], no significant increase in the MSD was observed in $Zr_{72}O_{143}\square$ when starting from the dynamically stable *Pbcn* structure (Fig. 3-2(a), red line). It is speculated that this discrepancy emerged because of the difference in the initial structures used for the current and previous studies. To reproduce the results of the previous studies and clarify the origin of the discrepancy, the MSD was also calculated starting from *cubic* ZrO_2 with *a,b*-axes tensile strain (*I4/mmm*) and without strain (*Fm-3m*), as assumed in previous studies [94][95]. As indicated by the red and purple lines (with/without strain) in Fig. 3-4, the enhanced MSD under tensile strain was reproduced.

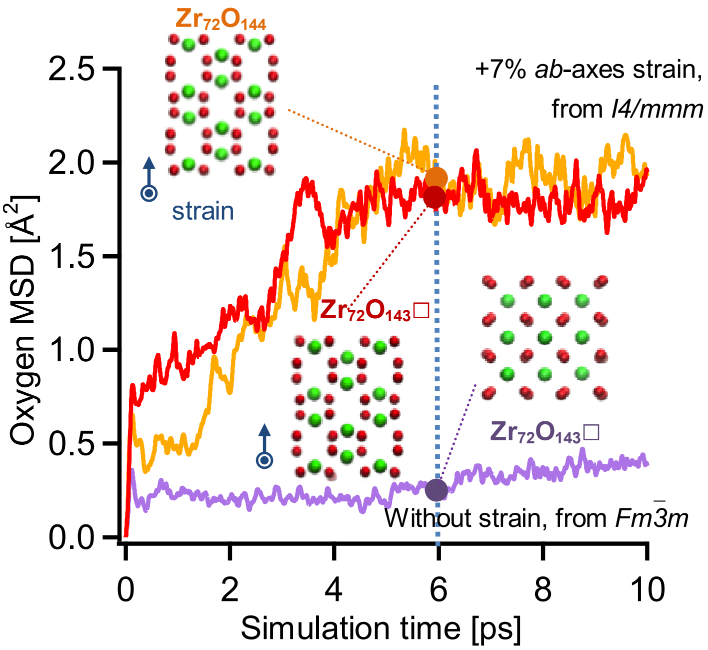

Fig. 3-4 MSDs of oxide ions starting from the cubic structure for zirconia with and without 7% *a,b*-axes tensile strain. Inset: optimized (at $T = 0$) structures whose initial structure was taken from the trajectory at $t = 6$ ps.

Notably, the increase in the MSD terminated after 6 ps, at which point the simulation time was halted in the previous studies. The inset of Fig. 3-4 shows the optimized structures (at $T = 0$) taken from the MD trajectory at $t = 6$ ps, which nearly coincide with the dynamically stable structures obtained using phonon calculations. Considering the energy difference between the initial structure and the stable structure, the MSD at 0–6 ps must represent the relaxation from the initial atomic positions. This observation was further corroborated by the results for the cell without Vo ($Zr_{72}O_{144}$, yellow line in Fig. 3-4). The MSD exhibited very similar behavior regardless of the elimination of V_O, which indicated that the increase in the MSD did not correspond to diffusion via the oxygen vacancy.

Conversely, the ionic conductivity was remarkably increased when the tensile strain and several oxygen vacancies were introduced simultaneously (Fig. 3-2(a), blue line). The magnitude of the increased MSD was greater than that expected from the increase in the oxygen vacancies ($1V_O$ to $6V_O$). In the unstrained system, though, the number of oxygen vacancies did not correspond in any obvious way to the oxide ion diffusion. The diffusion of oxide ion was negligible even at 2000 K, and differences between samples with a different number of V_O were not observed. This result indicates that the ionic conductivity was enhanced only when the lattice strain and oxygen vacancies cooperated. In addition, no effect of Y doping was observed under tensile strain along the *a*- and *b*-axes (Fig. 3-2(a)) when the lattice constants were locked to that of $SrTiO_3$. The MSD was relatively larger in the Y-doped unstrained cell (Fig. 3-2(b)), whose lattice constant was enlarged by the addition of Y^{3+}.

Figure 3-5 summarizes these diffusion coefficients, including the experimental ([50][86][87], [101]-[104]) and calculated values ([93]-[95]) reported to date. The experimental values in Fig. 3-5 were either determined directly using the oxygen tracer diffusion method or indirectly *via* conversion of electrochemical impedance spectroscopy data, denoted as EIS. Conversion from EIS data to the diffusion coefficients was performed using the Nernst-Einstein relation (Section 2.6.2), assuming that all of the oxide ions with a nominal charge of -2 contributed to the conduction. The previous studies experimentally compare the effect of a +3.04% (-4.37%) strain at the interface with Y_2O_3 (Sc_2O_3) in YSZ thin films [86][50]. As can be seen in Fig. 3-5, the tensile (compressive) strain increased (decreased) the diffusion. In the present study, the calculated enhancement of oxide ion diffusion ranged from several times to tenfold, which is consistent with their results and analytical expectation [92].

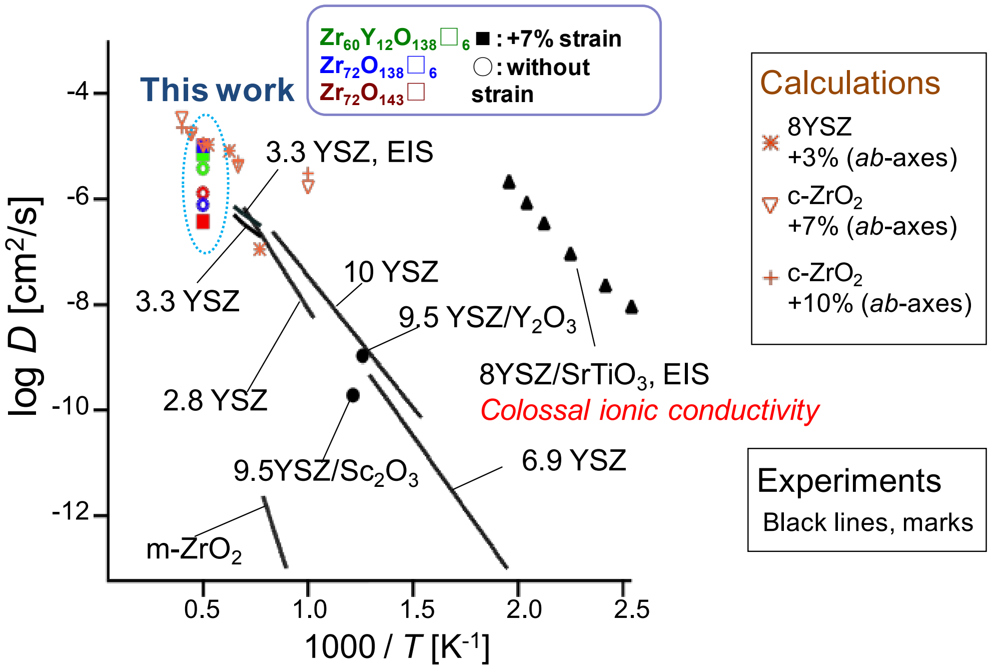

Fig. 3-5 Diffusion coefficient D obtained from the MSD plots for zirconia ('m' for monoclinic) and YSZ, where the numbers represent the concentration of yttria in zirconia. The colors of the marks correspond to those in Fig. 3-3 ($Zr_{72}O_{143}\square$: red, $Zr_{72}O_{138}\square_6$: blue, and $Zr_{60}Y_{12}O_{138}\square_6$: green), where filled and open symbols denote the samples with and without tensile strain, respectively. The data was extracted from Ref. [50][86][87], [101]-[104] (experiment) and [93]-[95] (calculation).

With regard to the controversy over the origin of colossal ionic conduction reported for YSZ/$SrTiO_3$, the present results provide a more reasonable value for the increased ionic conductivity of that system, which is caused by the cooperative effects of strain and oxygen vacancies.

3.3.3 Relationship between the structural change in the oxygen ordering and the ionic conductivity

The origin of the enhanced oxide ion conductivity with both strain and oxygen vacancies was investigated in terms of the positions of the cations and anions. Figure 3-6(a–f) depicts the optimized structures at $T = 0$ K obtained from the structures after the *ab initio* MD simulation of 2 ps (i.e. after increasing the temperature from 500 K to 2000 K) and the oxide ion trajectories (gray lines) in the three systems ($Zr_{72}O_{143}\square$, $Zr_{72}O_{138}\square_6$, and $Zr_{60}Y_{12}O_{138}\square_6$) with and without strain. The red, green, and dark green circles represent O^{2-}, Zr^{4+}, and Y^{3+} ions, respectively.

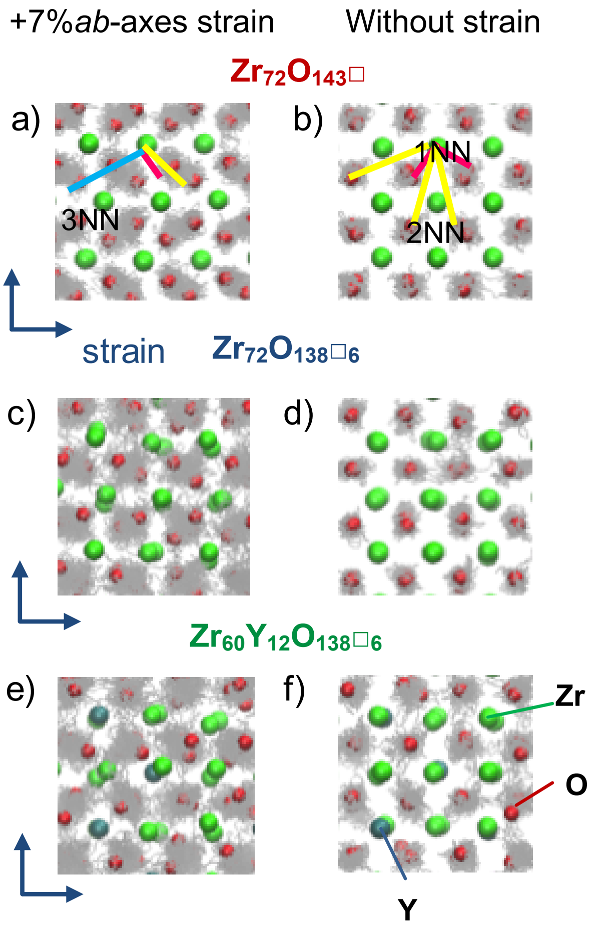
+7%ab-axes strain
Without strain
$Zr_{72}O_{143}\square$
a)
b)
1NN
2NN
3NN
strain
$Zr_{72}O_{138}\square_6$
c)
d)
$Zr_{60}Y_{12}O_{138}\square_6$
e)
f)
Zr
O
Y

Fig. 3-6 Stable structures at $T = 0$ obtained from the structures after the *ab initio* MD simulation of 2 ps (i.e. after increasing the temperature from 500 K to 2000 K) and oxide ion trajectories (gray lines) in the three systems ($Zr_{72}O_{143}\square$, $Zr_{72}O_{138}\square_6$, and $Zr_{60}Y_{12}O_{138}\square_6$) with strain ((a), (c), and (e)) and without strain ((b), (d), and (f)), respectively.

Figure 3-6(a) and (b) compares the effect of strain present in the model cell for $Zr_{72}O_{143}\square$. The solid lines in the figure represent the first (1NN), second (2NN), and third (3NN) nearest-neighbor Zr–O pairs. It was expected that the introduction of tensile strain would enlarge the Zr–O distances, i.e., weaken the bonds, and thus enhance oxide ion diffusion. However, under tensile strain, the Zr–O distance was not increased, but a new oxygen sublattice was formed. This behavior was also confirmed by examining the radial distribution functions (RDFs) of Zr–O (Fig. 3-7).

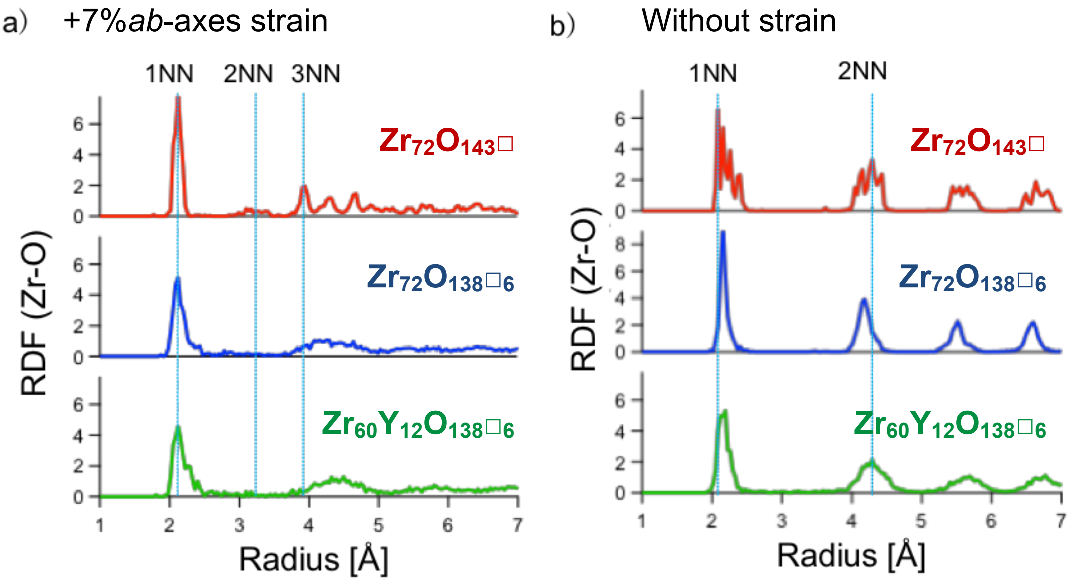

Fig. 3-7 RDFs of Zr–O corresponding to (a)–(f) in Fig. 3-6.

The RDF was drawn from one frame of the structure, as described in Fig. 3-6. In the unstrained $Zr_{72}O_{143}\square$ cell (red line in Fig. 3-7(b)), 1NN (around r = 2.09 Å) and 2NN peaks (around r = 4.29 Å) were observed. After application of the tensile strain along the a- and b-axes (red line in Fig. 3-7(a)), the 1NN peaks merged into a single peak (r = 2.12 Å), and new 2NN (around r = 3.24 Å) and 3NN peaks (r = 3.94 Å) appeared with lengths shorter than the 2NN peaks in the unstrained cell. These results indicate the formation of a rigid ordered structure composed of Zr and O atoms.

The situation differed when the cells contained several oxygen vacancies ($Zr_{72}O_{138}\square_6$) or doped Y ions ($Zr_{60}Y_{12}O_{138}\square_6$). In these cells, the oxygen sublattice was distorted, as depicted in Fig. 3-6(c) and (e), respectively. Simultaneously, the 1NN and other RDF peaks became broader (blue and green lines in Fig. 3-7(a)) than those for $Zr_{72}O_{143}\square$, which suggested that variation in the oxygen–cation bonds introduced flexibility into the system and promoted oxide ion diffusion. As described in Chapter 1, the mixed bonding character is one of the important factors for higher ionic conductivity, as it balances the stability of the mobile ions via several different co-ordinations during the diffusion process [1]. This expectation is consistent with the wandering trajectories of the oxide ions obtained from the *ab initio* MD simulations, as shown in Fig. 3-6(c) and (e). Therefore, it is proposed that the RDF for Zr–O in the optimized structure at $T = 0$ is a good indicator of the oxide ionic conductivity.

Note that the introduction of oxygen vacancies alone did not induce such deformation in the oxygen sublattice (Fig. 3-6(d)). In the unstrained Y^{3+} doped sample (Fig. 3-6(f)), however, a somewhat disordered oxygen sublattice was observed. This behavior explains the relatively high diffusion coefficient of oxide ion in $Zr_{60}Y_{12}O_{138}\square_6$, even without strain. Thus, the present results demonstrate that the ionic conductivity of ZrO_2 can be enhanced by the combined effects of oxygen sublattice formation induced by strain and further deformation of this sublattice by oxygen vacancies. The introduction of such disorder into the lattice by the aforementioned methods could be an important strategy for the enhancement of ionic conductivity.

In preceding studies, there are many polymorphs of pure ZrO_2 including the condition under hydrostatic pressure, which are predicted by theoretical calculations [105]-[108]. Among them, only five polymorphs have been reported experimentally: monoclinic ($P2_1/c$), tetragonal ($P4_2/nmc$), cubic ($Fm\bar{3}m$), and two high-pressure orthorhombic structures (*Pbca* and *Pnma*) [107][109]. Whereas the phase transition from cubic to tetragonal is driven by one phonon mode (X_2^-), there is no primary phonon mode to drive the phase transition from tetragonal to monoclinic directly [108]. Recent theoretical study revealed that this phase transition is driven by several phonon modes of Γ_3^+, M_1 and M_3, and that the M_1 mode induces the transition into *Pbcn* structure from tetragonal structure [108]. This *Pbcn* structure is the same as the dynamically stable structure under in-plane tensile strain obtained in this study. The calculated result of this study showed that the *Pbcn* structure was instable against cubic structure by 0.06 eV/f.u. The relationship of phase stability is summarized in Fig. 3-8.

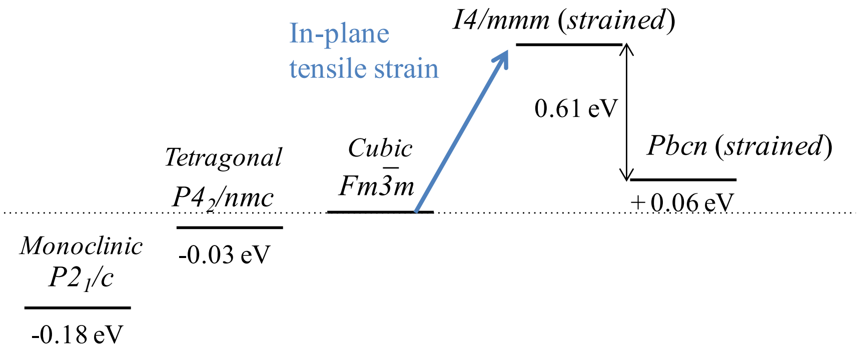

Fig. 3-8 The relationship of phase stability calculated in this study.

This relatively stable *Pbcn* structure suggests the possibility of another phase of ZrO_2, which can be easily stabilized by in-plane tensile strain. It might be possible to stabilize this *Pbcn* phase by other approaches such as arranging the ionic radii of anion/cation or tuning the hydrostatic pressure. Such investigation may provide wider application of ionic conductor with high conductivity.

3.4 Summary of this chapter

In this study, I performed DFT-based *ab initio* MD simulations for ZrO_2 systems to elucidate the origin of the colossal ionic conduction reported for the YSZ/$SrTiO_3$ heterostructure. I investigated how the ionic conduction in ZrO_2 systems is affected by three factors: strain, oxygen vacancies, and dopants. DFPT-based phonon calculations were performed to determine the dynamically stable structure of pure ZrO_2 under 7% tensile strain along the *a*- and *b*-axes. This structure adopts the space group *Pbcn* (referred to as zigzag structure), not *I4/mmm* of tensile-strained cubic ZrO_2. Thus, previous theoretical studies that assumed the same structure as cubic ZrO_2 for YSZ may have overestimated the ionic conductivity due to relaxation from their initial structures (*I4/mmm*) to this stable structure (*Pbcn*). It is speculated that the breakdown of zigzag structure of ZrO_2 during the MD simulation, reported previously [94], is the relaxation process from the initial cubic structure.

Ab initio MD simulations were performed for the following three samples, focusing on the individual effect of the corresponding factor: strain ($Zr_{72}O_{143}\square$), vacancies ($Zr_{72}O_{138}\square_6$), and dopants ($Zr_{60}Y_{12}O_{138}\square_6$). Starting from dynamically stable structure, zigzag structure of ZrO_2 retained at 2000 K and no enhancement of oxide ion diffusion was observed by tensile strain alone. On the other hand, a significant increase was observed when the tensile strain and oxygen vacancies were introduced simultaneously ($Zr_{72}O_{138}\square_6$ and $Zr_{60}Y_{12}O_{138}\square_6$). Evaluation of the RDF for Zr–O in the stable structure revealed that a new oxygen sublattice was formed under tensile strain and that this structure was further distorted by oxygen vacancies. The breakdown of the zigzag structure of ZrO_2 was achieved only when several oxygen vacancies are combined. Therefore, formation of the new oxygen sublattice due to tensile strain and its distortion by oxygen vacancies both play a crucial role in the increase in oxide ion conductivity in these systems.

Chapter 4 *Ab initio* MD simulation of N/F-doped ZrO_2 under epitaxial strain

本章については、５年以内に雑誌等で刊行予定のため、非公開。

Chapter 5 DFT-based first-principles simulations of LaOF

本章については、５年以内に雑誌等で刊行予定のため、非公開。

Chapter 6 General conclusion

In this thesis, I discussed the mechanism of ionic conduction and explored the keys to control their properties based on the first-principles simulations. I focused on two materials having fluorite structure, ZrO_2 and LaOF.

In Chapter 3, I investigated the mechanism of the ionic conduction in ZrO_2 systems under tensile epitaxial strain. I conducted density functional perturbation theory (DFPT)-based phonon calculations to determine the dynamically stable structure. The oxygen sublattice of ZrO_2 was dramatically changed into the zigzag structure (space group of *Pbcn*) by tensile epitaxial strain. *Ab initio* MD simulations were performed initiating from the dynamically stable structure. The ionic conductivity was remarkably increased when the tensile strain and several oxygen vacancies were introduced simultaneously. The conductivity was almost dominated by the number of oxygen vacancies. These oxygen vacancies seemingly deformed the spatial oxygen ordering state, which led to the enhancement of the ionic conductivity of oxide ion. The present results indicate that the oxide ion conductivity in ZrO_2 is largely influenced by the oxygen ordering pattern, which sensitively changes with the lattice strain and the number of oxygen vacancies.

In Chapter 4, I discussed the effect of N/F-doping into tensile-strained ZrO_2, from the structural change of oxygen sublattice. The effect of N/F-doping was further analyzed referring to the strengths of Zr–O bonds. Under tensile strain, the zigzag structure of pure ZrO_2 was broken by the anion dopants or oxygen vacancies. The zigzag structure was perturbed by the flipping motion of the lattice at low concentration of dopants or vacancies, and, with increasing the concentration, it was broken into a fluid-like state. Besides, chemical bonding analysis of Zr−O showed that the bonds near the vacancies was weakened by F- or V_O-doping and strengthened by

N-doping. Despite the opposite effects on the near-by Zr−O bonds, all doping commonly enhanced the ionic conduction; the doped F^- or V_O directly weakened the Zr–O bonds in its vicinity, whereas the N^{3-} strengthened the Zr–O bonds in its vicinity but weakened other Zr–O bonds and thus promoted the ionic conduction.

The results of ZrO_2 systems were reviewed in terms of the migration path and its barrier height. Without strain, ZrO_2 showed only vacancy mechanism, which was corroborated by the calculated migration energies of vacancy and interstitialcy mechanisms. Under the in-plane tensile strain, migration barrier of the interstitialcy mechanism became much lower than in unstrained case. This observation suggests that the interstitial sites were opened by the tensile strain, which reduces the migration barrier of interstitialcy mechanism in ZrO_2 systems. Additionally, I observed a peculiar migration mechanism, which is similar to the vacancy mechanism but is mediated by the interstitial position. This migration mechanism *via* interstitial site might be easier to occur in the in-plane direction than in the out-of-plane, since the interstitial site is opened along the in-plane direction by the tensile strain. This novel conducting mechanism involving interstitial sites, which were induced by tensile strain, supposedly contributed to the enhanced ionic conductivity in ZrO_2 systems.

Finally, in Chapter 5, I explored the ionic conduction mechanism on a mixed anion compounds LaOF, which shows fluoride ion conduction with high selectivity. The formation of F Frenkel pair was more energetically favored than O Frenkel pair by more than 1.7 eV, which suggests that the F Frenkel pair contributes to the fluoride ion conduction. *Ab initio* MD simulations revealed that the fluoride ion conduction was mainly mediated by the interstitialcy mechanism. Compared to ZrO_2 case, LaOF should have enough room for interstitial sites since large La^{3+} cations (r = 117 pm) compared to Zr^{4+} (r = 86 pm) might behave as spacers in the crystal, which opens the space for interstitial sites. Interestingly, such interstitialcy mechanism of interstitial fluoride ion occurred along (001) plane only when its nearest anion sites on the (001) plane are occupied by fluoride ions. The present finding, i.e., dominancy of the interstitialcy mechanism under a restricted condition, suggests that the ionic conductivity of mixed anion compounds can be enhanced by controlling the anion ordering.

In conclusion, present results suggest the possibility to control the ionic conducting mechanism by several factors such as strain, doping, or ordering of ions.

Bibliography

[1] S. Hull, Rep. Prog. Phys. **67**, 1233 (2004).

[2] R. D. Shannon, Acta Crystallogr. **A 32**, 751 (1976).

[3] M. Aniya, Solid State Ionics **70**, 673 (1994).

[4] W. Schröter and J. Nölting, J. Phys. Colloques **41**, C6 20 (1980).

[5] C. Pirovano M. S. Islam, R. N. Vannier, G. Nowogrocki, and G. Mairesse, Solid State Ionics **140**, 115 (2001).

[6] F. Abraham , J. C. Boivin, G. Mairesse, and G. Nowogrocki, Solid State Ionics **40-1**, 934 (1990).

[7] J. L. Soubeyroux, J. M. Reau, S. Matar, G. Villeneuve, and P. Hagenmuller, Solid State Ionics **6**, 103 (1982).

[8] 黒沢達美著, 物性論: 固体を中心とした, 2002 年, 裳華房.

[9] Y. Arachi, H. Sakai, O. Yamamoto, Y. Takeda and N. Imanishai, Solid State Ionics **121**, 133 (1999).

[10] K. Kiukkola and C. Wagner, J. Electrochem. Soc. **104**, 379 (1957).

[11] H. Merler, *Diffusion in solids: fundamentals, methods, materials, diffusion-controlled processes* (Springer, 2007).

[12] D. Marrocchelli, P. A. Madden, S. T. Norberg, and S. Hull, Chem. Mater. **23**,

1365 (2011).

[13] K. Compaan and Y. Haven, Trans. Faraday Soc. **52**, 786 (1956).

[14] K. Compaan and Y. Haven, Trans. Faraday Soc. **54**, 1498 (1958).

[15] L. Malavasi, C. A. J. Fisher, and M. S. Islam, Chem. Soc. Rev. **39**, 4370 (2010).

[16] K. Fujii, Y. Esaki, K. Omoto, M. Yashima, A. Hoshikawa, T. Ishigaki, and J. R. Hester, Chem. Mater. **26**, 2488 (2014).

[17] G. Kobayashi, Y. Hinuma, S. Matsuoka, A. Watanabe, M. Iqbal, M. Hirayama, M. Yonemura, T. Kamiyama, I. Tanaka, and R. Kanno, Science **351**, 1314 (2016).

[18] P. Aldebert and J. P. Traverse, J. Am. Ceram. Soc. **68**, 34 (1985).

[19] R. A. De Souza, A. Ramadan, and S. Horner, Energy Environ. Sci. **5**, 5445 (2012).

[20] M. Nolan, J. Phys. Chem. C **115**, 6671 (2011).

[21] J. Holsa, E. Sailynoja, P. Ylha, P. Porcher, P. Deren, and W. Strek, J. Phys. Chem. **100**, 14736 (1996)

[22] J. Holsa, E. Sailynoja, P. Ylha, E. Antic-Fidancev, M. Lemaitre-Blaise, and P. Porcher, J. Chem. Soc.-Faraday Tran. **94**, 481 (1998).

[23] K. Niihara and S. Yajima, Bull. Chem. Soc. Jpn. **44**, 643 (1971).

[24] K. T. Jacob, V. S. Saji, and Y. Waseda, Int. J. Appl. Ceram. Technol. **3**, 312

(2006).

[25] B. Liu, H. Y. Xiao, Y. W. Zhang, D. S. Aidhy, and W. J. Weber, Comput. Mater. Sci. **92**, 22 (2014).

[26] S. Beschnitt, T. Zacherle, and R. A. De Souza, J. Phys. Chem. C **119**, 27307 (2015).

[27] W. Bollmann and R. Reimann, Phys. Status Solidi A **16**, 187 (1973).

[28] P. Jain, S. Kim, R. E. Youngman, and S. Sen, J. Phys. Chem. Lett. **1**, 1126 (2010).

[29] T. Ishihara, H. Matsuda, and Y. Takita, J. Am. Chem. Soc. **116**, 3801 (1994).

[30] A. Chroneos, B. Yildiz, A. Tarancon, D. Parfitt, and J. A. Kilner, Energy Environ. Sci. **4**, 2774 (2011).

[31] A. Aguadero, L. Fawcett, S. Taub, R. Woolley, K.-T. Wu, N. Xu, J. A. Kilner, and S. J. Skinner, J. Mater. Sci. **47**, 3925 (2012).

[32] M. Yashima, H. Yamada, S. Nuansaeng, and T. Ishihara, Chem. Mater. **24**, 4100 (2012).

[33] M. Sase, K. Yashiro, K. Sato, J. Mizusaki, T. Kawada, N. Sakai, K. Yamaji, T. Horita, and H. Yokokawa, Solid State Ionics **178**, 1843 (2008).

[34] A. Kushima, D. Parfitt, A. Chroneos, B. Yildiz, J. A. Kilner, and R. W. Grimes, Phys. Chem. Chem. Phys. **13**, 2242 (2011).

[35] A. Orera and P. R. Slater, *Chem. Mater.* **22**, 675 (2010).

[36] B. N. Pal, B. M. Dhar, K. C. See, and H. E. Katz, Nature Mater. **8**, 898 (2009).

[37] J. C. Bachman, S. Muy, A. Grimaud, H. H. Chang, N. Pour, S. F. Lux, O. Paschos, F. Maglia, S. Lupart, P. Lamp, L. Giordano, and Y. Shao-Horn, Chem. Rev. **116**, 140 (2016).

[38] D. J. L. Brett, A. Atkinson, N. P. Brandon, and S. J. Skinner, Chem. Soc. Rev. **37**, 1568 (2008).

[39] J.-M. Tarascon and M. Armand, Nature **414**, 359 (2001).

[40] M. Anji Reddy and M. Fichtner, J. Mater. Chem. **21**, 17059 (2011).

[41] B. C. H. Steele and A. Heinzel, Nature **414**, 345 (2001).

[42] A. Evans, A. Bieberle-Hütter, and J.L.M. Rupp, L.J. Gauckler, J. Power Sources **194**, 119 (2009).

[43] N. Mahato, A. Banerjee, A. Gupta, S. Omar, and K. Balani, Prog. Mater. Sci. **72**, 141 (2015).

[44] S.B. Adler, Solid State Ionics **111**, 125 (1998).

[45] N. Williard, W. He, C. Hendricks, and M. Pecht, Energies **6**, 4682 (2013).

[46] P. E. Ross, IEEE Spectrum **50**, 11 (2013).

[47] C. Rongeat, M.A. Reddy, R. Witter, and M. Fichtner, J. Phys. Chem. C **117**, 4943 (2013).

[48] L. Zhang, M. A. Reddy, and M. Fichtner, Solid State Ionics **272**, 39 (2015).

[49] F. Gschwind, G. Rodriguez-Garcia, D. J. S. Sandbeck, A. Gross, M. Weil, M. Fichtner, and N. Hormann, J. Fluorine Chem. **182**, 76 (2016).

[50] H. Aydin, C. Korte, M. Rohnke, and J. Janek, Phys. Chem. Chem. Phys. **15**, 1944 (2013).

[51] M. Gerstl, T. Fromling, A. Schintlmeister, H. Hutter, and J. Fleig, Solid State Ionics **184**, 23 (2011).

[52] Q.-A. Huang, R. Hui, B. Wang, and H. Zhang, Electrochimica Acta **52**, 8144 (2007).

[53] M. Gerstl, G. Friedbacher, F. Kubel, H. Hutter, and J. Fleig, Phys. Chem. Chem. Phys. **15**, 1097 (2013).

[54] J. E. Auckett, A. J. Studer, E. Pellegrini, J. Ollivier, M. R. Johnson, H. Schober, W. Miiller, and C. D. Ling, Chem. Mater. **25**, 3080 (2013).

[55] K. L. Duncan, E.D. Wachsman, Ionics **13**, 127 (2007).

[56] J. Maier, Angew. Chem. Int. Ed. **52**, 4998 (2013).

[57] 岡崎進・吉井範行著，コンピュータ・シミュレーションの基礎, 2011 年, 化学同人.

[58] T. Hoshi, K. Yamazaki, and Y. Akiyama, JPS Conf. Proc. **1**, 016004 (2014).

[59] P. Hohenberg and W. Kohn, Phys. Rev. **136 (3B)**, B864 (1964).

[60] W. Kohn and L. J. Sham, Phys. Rev. **140 (4A)**, A1133 (1965).

[61] 小口多美夫著, バンド理論, 1999 年, 内田老鶴圃.

[62] J. Hafner (2003), “Foundations of density-functional theory” (Hands-on tutorial course on VASP), [online] https://www.vasp.at/vasp-workshop/slides/dft_introd.pdf#search=%27 kohn+sham+theory+vasp%27

[63] J. Heyd, G. E. Scuseria, and M. Ernzerhof, J. Chem. Phys. **118**, 8207 (2003).

[64] J. Heyd, G. E. Scuseria, and M. Ernzerhof, J. Chem. Phys. **124**, 219906 (2006).

[65] Z. Wu and R. E. Cohen, *Phys. Rev. B* **73**, 235116 (2006).

[66] J. P. Perdew, K. Burke, and M. Ernzerhof, Phys. Rev. Lett. **77**, 3865 (1996).

[67] P. E. Blöchl, Phys. Rev. B: Condens. Matter Mater. Phys. **50**, 17953 (1994).

[68] H. J. Monkhorst and J. D. Pack, Phys. Rev. B: Condens. Matter Mater. Phys. **13**, 5188 (1976).

[69] G. Kresse and J. Furthmuller, Phys. Rev. B: Condens. Matter Mater. Phys. **54**, 11169 (1996).

[70] P. Giannozzi, *et al.*, J. Phys.: Condens. Matter **21**, 395502 (2009).

[71] B.-T. Wang, P. Zhang, H.-Y. Liu, W.-D. Li, and P. Zhang, J. Appl. Phys. **109**, 6 (2011).

[72] S. Lany and A. Zunger, *Phys. Rev. B* **78**, 235104 (2008).

[73] W. Araki and Y. Arai, Solid State Ionics **190**, 75 (2011).

[74] C. R. A. Catlow, J. Corish, and P. W. M. Jacobs, J. Phys. C-Solid State Physics **12**, 3433 (1979).

[75] K. Park and D. R. Olander, J. Electrochem. Soc. **138**, 1154 (1991).

[76] A. Kushima and B. Yildiz, J. Mater. Chem. **20**, 4809 (2010).

[77] T. Hughbanks and R. Hoffmann, J. Am. Chem. Soc. **105**, 3528 (1983).

[78] R. Dronskowski and P. E. Blochl, J. Phys. Chem. **97**, 8617 (1993).

[79] V. L. Deringer, A. L. Tchougreeff, and R. Dronskowski, J. Phys. Chem. A **115**, 5461 (2011).

[80] S. Maintz, V. L. Deringer, A. L. Tchougreeff, and R. Dronskowski, J. Comput. Chem. **34**, 2557 (2013).

[81] S. Maintz, V. L. Deringer, A. L. Tchougreeff, and R. Dronskowski, J. Comput. Chem. **37**, 1030 (2016).

[82] D. Sheppard, R. Terrell, and G. Henkelman, J. Chem. Phys. **128**, 134106 (2008).

[83] D. Sheppard, P. Xiao, W. Chemelewski, D. D. Johnson, and G. Henkelman, J. Chem. Phys. **136**, 074103 (2012).

[84] http://theory.cm.utexas.edu/vtsttools/index.html

[85] N. Sata, K. Eberman, K. Eberl, and J. Maier, Nature **408**, 946 (2000).

[86] H. Aydin, C. Korte, and J. Janek, Sci. Technol. Adv. Mater. **14**, 035007 (2013).

[87] J. Garcia-Barriocanal, A. Rivera-Calzada, M. Varela, Z. Sefrioui, E. Iborra, C. Leon, S. J. Pennycook, and J. Santamaria, Science **321**, 676 (2008).

[88] X. Guo, Science **324**, 465a (2009).

[89] A. Cavallaro, M. Burriel, J. Roqueta, A. Apostolidis, A. Bernardi, A. Tarancon, R. Srinivasan, S. N. Cook, H. L. Fraser, J. A. Kilner, D. W. McComb, and J. Santiso, Solid State Ionics **181**, 592 (2010).

[90] R. A. De Souza and A. H. H. Ramadan, Phys. Chem. Chem. Phys. **15**, 4505 (2013).

[91] E. Fabbri, D. Pergolesi, and E. Traversa, Sci. Technol. Adv. Mater. **11**, 054503 (2010).

[92] C. Korte, J. Keppner, A. Peters, N. Schichtel, H. Aydin, and J. Janek, Phys. Chem. Chem. Phys. **16**, 24575 (2014).

[93] G. Dezanneau, J. Hermet, and B. Dupe, Int. J. Hydrogen Energy **37**, 8081 (2012).

[94] T. J. Pennycook, M. J. Beck, K. Varga, M. Varela, S. J. Pennycook, and S. T. Pantelides, Phys. Rev. Lett. **104**, 115901 (2010).

[95] F. Li, R. Lu, H. Wu, E. Kan, C. Xiao, K. Deng, and D. E. Ellis, Phys. Chem. Chem. Phys. **15**, 2692 (2013).

[96] M. I. Aroyo, J. M. Perez-Mato, C. Capillas, E. Kroumova, S. Ivantchev, G. Madariaga, A. Kirov, and H. Wondratschek, Z. Kristallogr. **221**, 15 (2006).

[97] A. Togo, F. Oba and I. Tanaka, Phys. Rev. B: Condens. Matter Mater. Phys. **78**, 134106 (2008).

[98] K. Parlinski, Z. Q. Li, and Y. Kawazoe, Phys. Rev. Lett. **78**, 4063 (1997).

[99] M. Sternik and K. Parlinski, J. Chem. Phys. **123**, 204708 (2005).

[100] A. Kuwabara, T. Tohei, T. Yamamoto, and I. Tanaka, Phys. Rev. B: Condens. Matter Mater. Phys. **71**, 064301 (2005).

[101] A. Madeyski and W. W. Smeltzer, Mater. Res. Bull. **3**, 369 (1968).

[102] U. Brossmann, G. Knoner, H. E. Schaefer, and R. Wurschum, Rev. Adv. Mater. Sci. **6**, 7 (2004).

[103] B. K. Kim, S. J. Park, and H. Hamaguchi, J. Am. Ceram. Soc. **76**, 2119 (1993).

[104] M. Kilo, C. Argirusis, G. Borchardt, and R. A. Jackson, Phys. Chem. Chem. Phys. **5**, 2219 (2003).

[105] H. Öztürk and M. Durandurdu, Phys. Rev. B **79**, 134111 (2009).

[106] H. B. Wu, Y. F. Duan, K. Liu, D. Lv, L. X. Qin, L. W. Shi, and G. Tang, J. Alloys Compd. **645**, 352 (2015).

[107] W. Wang, Z. Z. Liang, X. L. Han, J. F. Chen, C. Y. Xue, and H. Zhao, J. Alloys Compd. **622**, 504 (2015).

[108] R. A. Evarestov and Y. E. Kitaev, J. Appl. Crystallogr. **49**, 1572 (2016).

[109] J. Haines, J. M. Leger, S. Hull, J. P. Petitet, A. S. Pereira, C. A. Perottoni, and J. A. H. da Jornada, J. Am. Ceram. Soc. **80**, 1910 (1997).

[110] J. S. Lee, M. Lerch, and J. Maier, J. Solid State Chem. **179**, 270 (2006).

[111] I. Valov, R. A. De Souza, C. Z. Wang, A. Boerger, C. Korte, M. Martin, K. D. Becker, and J. Janek, J. Mater. Sci. **42**, 1931 (2007).

[112] I. Valov, V. Ruehrup, R. Klein, T. C. Roedel, A. Stork, S. Berendts, M. Dogan, H. D. Wiemhoefer, M. Lerch, and J. Janek, Solid State Ionics **180**, 1463 (2009).

[113] T. Bredow, Physical Review B **75**, 144102 (2007).

[114] M. O. Zacate, L. Minervini, D. J. Bradfield, R. W. Grimes, and K. E. Sickafus, Solid State Ionics **128,** 243 (2000).

[115] K. K. Deb, R. G. Buser, C. A. Morrison, and R. P. Leavitt, J. Opt. Soc. Am. **71**, 1463 (1981).

[116] Q. Xie, Y. Wang, B. Pan, H. Wang, W. Su, and X. Wang, Catal. Commun. **27**, 21 (2012).

[117] M. Shang, D. Geng, X. Kang, D. Yang, Y. Zhang, and J. Lin, Inorg. Chem. **51**, 11106 (2012).

[118] T. Grzyb, M. Weclawiak, T. Pedzinski, and S. Lis, Opt. Mater. **35**, 2226 (2013).

[119] L. Tao, W. Xu, Y. Zhu, L. Xu, H. Zhu, Y. Liu, S. Xu, P. Zhou, and H. Song, J. Mater. Chem. C **2**, 4186 (2014).

[120] B. Shao, Q. Zhao, W. Lv, M. Jiao, W. Lue, and H. You, Adv. Optical Mater. **3**, 583 (2015).

[121] J. W. Fergus and H. P. Chen, J. Electrochem. Soc. **147**, 4696 (2000).

[122] M. Ando, M. Enoki, H. Nishiguchi, T. Ishihara, and Y. Takita, Chem. Mater. **16**, 4109 (2004).

[123] M. Takashima, J. Fluorine Chem. **105**, 249 (2000).

[124] J. Holsa, E. Sailynoja, H. Rahiala, and J. Valkonen, Polyhedron **16**, 3421 (1997).

[125] S. Heiroth, T. Lippert, A.Wokaun, M. Döbeli, J.L.M. Rupp, B. Scherrer, and L.J. Gauckler, J. Eur. Ceram. Soc. **30**, 489 (2010).